## **OPEN ACCESS**



# Characterizing Extreme Emission Line Galaxies. II. A Self-consistent Model of Their Ionizing Spectrum\*

Grace M. Olivier <sup>1,2</sup>, Danielle A. Berg <sup>3</sup>, John Chisholm <sup>3</sup>, Dawn K. Erb <sup>4</sup>, Richard W. Pogge <sup>1,2</sup>, and Evan D. Skillman <sup>5</sup>, Department of Astronomy, The Ohio State University, 140 W. 18th Avenue, Columbus, OH 43210, USA; grace.m.olivier@gmail.com <sup>2</sup> Center for Cosmology & AstroParticle Physics, The Ohio State University, 191 W Woodruff Avenue, Columbus, OH 43210, USA <sup>3</sup> Department of Astronomy, The University of Texas at Austin, 2515 Speedway, Stop C1400, Austin, TX 78712, USA <sup>4</sup> The Leonard E. Parker Center for Gravitation, Cosmology and Astrophysics, Department of Physics, University of Wisconsin-Milwaukee, 3135 North Maryland Avenue, Milwaukee, WI 53211, USA

Minnesota Institute for Astrophysics, University of Minnesota, 116 Church Street SE, Minneapolis, MN 55455, USA Received 2021 September 14; revised 2022 May 27; accepted 2022 June 10; published 2022 October 11

#### Abstract

Observations of high-redshift galaxies (z > 5) have shown that these galaxies have extreme emission lines with equivalent widths much larger than their local star-forming counterparts. Extreme emission line galaxies (EELGs) in the nearby universe are likely analogs to galaxies during the Epoch of Reionization and provide nearby laboratories to understand the physical processes important to the early universe. We use Hubble Space Telescope/ Cosmic Origins Spectrograph and Large Binocular Telescope/Multi-Object Double Spectrographs spectra to study two nearby EELGs, J104457 and J141851. The far-UV spectra indicate that these two galaxies contain stellar populations with ages  $\leq 10$  Myr and metallicities  $\leq 0.15 Z_{\odot}$ . We use photoionization modeling to compare emission lines from models of single-age bursts of star formation to observed emission lines and find that the single-age bursts do not reproduce high-ionization lines including [O III] or very-high-ionization lines like He II or O IV]. Photoionization modeling using the stellar populations fit from the UV continuum similarly is not capable of reproducing the very-high-energy emission lines. We add a blackbody to the stellar populations fit from the UV continuum to model the necessary high-energy photons to reproduce the very-high-ionization lines of He II and O IV]. We find that we need a blackbody of 80,000 K and  $\sim 45\%-55\%$  of the luminosity from the blackbody and young stellar population to reproduce the very-high-ionization lines while simultaneously reproducing the low-, intermediate-, and high-ionization emission lines. Our self-consistent model of the ionizing spectra of two nearby EELGs indicates the presence of a previously unaccounted-for source of hard ionizing photons in reionization analogs.

*Unified Astronomy Thesaurus concepts*: Dwarf galaxies (416); Ultraviolet astronomy (1736); Galaxy chemical evolution (580); Galaxy spectroscopy (2171); High-redshift galaxies (734); Emission line galaxies (459)

Supporting material: data behind figure

## 1. Introduction

The first galaxies are likely responsible for producing the photons that ionized the universe during the Epoch of Reionization (EoR; Wise et al. 2014; Robertson et al. 2015; Madau & Haardt 2015; Stanway et al. 2016). With telescopes like the Hubble Space Telescope (HST) and Atacama Large Millimeter/submillimeter Array, among others, astronomers have discovered thousands of galaxies in the high-redshift universe (z > 6) in an attempt to study these first galaxies (e.g., Bouwens et al. 2015; Finkelstein et al. 2015; Livermore et al. 2017; Atek et al. 2018; Oesch et al. 2018; Bouwens et al. 2020; Harikane et al. 2020). More direct observations of these first galaxies and their environments during the EoR are just on the horizon with the coming era of the James Webb Space Telescope and extremely large telescopes, in combination with

Original content from this work may be used under the terms of the Creative Commons Attribution 4.0 licence. Any further distribution of this work must maintain attribution to the author(s) and the title of the work, journal citation and DOI.

next-generation HI surveys such as the Square Kilometer Array. Soon we will be able to observe the first galaxies and their effects on the neutral gas surrounding them.

Over the past decade, the rest-frame UV emission-line spectra have been observed from several very-high-redshift galaxies (z > 6) revealing strong, high-ionization nebular lines (e.g., Stark et al. 2015; Stark 2016; Mainali et al. 2018) that are indicative of very hard radiation fields in low-metallicity environments. With this in mind, much can be learned from detailed studies of nearby galaxies with properties analogous to what we expect to find in the distant universe. In particular, recent studies have focused on metal-poor, high-ionization galaxies with high specific star formation rates (sSFRs) both locally (e.g., Berg et al. 2016; Izotov et al. 2016; Jaskot et al. 2017; Senchyna et al. 2017; Izotov et al. 2018; Senchyna et al. 2020; Berg et al. 2019a, 2019b) and at intermediate redshifts using lensed galaxies (e.g., Hainline et al. 2009; Bayliss et al. 2014; Christensen et al. 2014; James et al. 2014; Rigby et al. 2018a; Berg et al. 2018).

These recently discovered samples of reionization analogs have extreme equivalent widths (EWs) in their emission lines from high-ionization species like O III], C III], C IV, and He II. As a result of their large EWs and hard radiation fields, extreme emission line galaxies (EELGs) in the local universe provide a laboratory for understanding the physical processes active in

<sup>\*</sup> Based on observations made with the NASA/ESA Hubble Space Telescope, obtained from the Data Archive at the Space Telescope Science Institute, which is operated by the Association of Universities for Research in Astronomy, Inc., under NASA contract NASA 5-26555.

the first galaxies. The large EWs from O III], C IV, and He II in galaxies out to  $z\sim2$  have been associated with low-metallicity environments and very young stellar populations from recent bursts of star formation producing highly ionized gas (Atek et al. 2011; van der Wel et al. 2011; Maseda et al. 2013, 2014; Rigby et al. 2015; Berg et al. 2016; Senchyna et al. 2017; Chevallard et al. 2018; Berg et al. 2019a, 2019b; Tang et al. 2019, 2021). Exploring similarly low-metallicity environments in local EELGs can help us understand those young stellar populations and the highly ionized gas.

These EELGs often demonstrate strong He II emission along with their other extreme emission lines, but the mechanisms producing the high-energy photons at >54 eV are rarely understood. A number of studies have explored the production mechanism for the extreme He II emission at  $\lambda$ 1640 in the restframe UV and  $\lambda$ 4686 in the optical in a number of these reionization analogs (e.g., Schaerer 2002; Kehrig et al. 2015, 2018, 2021; Schaerer et al. 2019; Senchyna et al. 2017, 2020). Some of the postulated sources of the He II emission include: Wolf–Rayet stars at low-metallicity, high-mass X-ray binaries, metal-poor massive stars, and shocks. But, when examined in more detail, these suggestions tend to be inadequate in their photon production in the energy range needed for extreme He II emission (Kehrig et al. 2015, 2018; Senchyna et al. 2020; Grasha et al. 2021; Wofford et al. 2021).

Here we examine two of these reionization era analog galaxies. The first of these galaxies is J104457, which has the largest C IV  $\lambda\lambda$  1548,1550 Å EW (-6.71 Å, -2.83 Å) measured in the local universe (Berg et al. 2016). The second galaxy is J141851, which has the largest He II  $\lambda$ 1640 Å EW  $(-2.82 \,\text{Å})$  measured in the local universe (Berg et al. 2019a). These two galaxies are prime targets for studying the physical processes required to create high-ionization gas and to explore the conditions present in the EoR. A preliminary study of the high-energy ionizing photons in these galaxies was presented in Berg et al. (2019b), but these fascinating objects demand a more complete analysis. Here we present the second paper in a series of work to characterize EELGs. In Berg et al. (2021, hereafter Paper I), we presented a detailed examination of the extreme emission lines, nebular physical conditions, and chemical abundances in J104457 and J141851. Owing to the detection of a number of very-high-ionization emission lines (e.g., C IV, He II, O IV], Si IV, [Ne V], and [Ar IV]), we adopted a novel four-zone ionization model and found both EELGs to be characterized by much higher ionization parameters than reported in previous works. The main result of Paper I highlights a persistent high-energy ionizing photon production problem (HEIP<sup>3</sup>) that motivates the self-consistent modeling of their ionizing spectra presented here in Paper II.

Paper II is structured as follows: We present the optical and UV spectra of J104457 and J141851 in Section 2. In Section 3, we investigate the UV stellar continuum. The procedure used for the stellar continuum fits is discussed in Section 3.1, and the resulting stellar population properties are presented in Section 3.2. Additionally, we generalize our findings in order to characterize the spectra of extremely metal-poor stellar populations in Section 3.3. Section 4 then combines constraints from the stellar continuum fits of Section 3 with the emission line ratios from the optical and UV spectra using CLOUDY (Ferland et al. 2017) photoionization modeling. We explore several input ionizing sources in Section 4.2, including single-aged burst binary models (Section 4.2.1), the best-fit stellar

population models (Section 4.2.2), and combined stellar plus blackbody models (Section 4.2.3). The resulting best fit to the suite of observed emission lines is produced by the latter models, requiring an additional source of very-high-energy ionizing photons. We discuss this result and the possible physical origin of the very-high-energy photons in Section 5. Finally, we present our conclusions in Section 6.

#### 2. Extreme UV Emission-line Galaxy Observations

The main objective of this work is to investigate whether the suite of nebular emission lines from two EELGs can be self-consistently reproduced by photoionization models using the ionizing photons from the massive star populations. To analyze the interplay of the ionizing stellar population and nebular gas of J104457 and J141851, we first measure the nebular emission lines from their UV and optical spectra.

## 2.1. HST/COS UV Spectra

In this work we used far-UV (FUV) spectra taken with the Cosmic Origins Spectrograph (COS) on the HST that were first reported in Berg et al. (2016, 2019a) and Berg et al. (2019b) from the HST Project ID 15465. We briefly summarize the observational details below.

All observations were centered on the near-UV (NUV) flux of J104457 and J141851 using the ACQ/Image acquisition mode. Science exposures were then taken in the TIME-TAG mode using the 2."5 PSA aperture. The FP-POS = ALL setting was used to take four images offset from one another in the dispersion direction, increasing the cumulative signal-to-noise ratio (S/N) and mitigating the effects of fixed pattern noise. Spectra were processed with CALCOS version 3.3.4, using the standard EXTRACTSEGMENTBOXCAR aperture method, and binned by the six native COS pixels per resolution element such that the nominal  $\delta v = 13.1 \ \text{km s}^{-1}$ .

The G160M spectra used a central wavelength of 1589 Å and had total exposures of 6439 and 12,374 s for J104457 and J141851, respectively. This setup provides wavelength coverage that is rich with stellar and nebular features. In particular, these spectra cover several important FUV high-ionization emission lines: Si IV  $\lambda\lambda 1394,1403$ , O IV]  $\lambda\lambda 1401,1405$ , 1407, S IV  $\lambda\lambda$ 1405,1406,1417,1424, N IV  $\lambda\lambda$ 1483,1487, C IV  $\lambda\lambda 1548$ , 1550, He II  $\lambda 1640$ , and O III]  $\lambda\lambda 1661,1666$ . For the purpose of testing the production of nebular emission lines, not only are the Si IV, C IV, and He II features difficult to interpret due to their potentially complex nebular and stellar contributions, but Si IV and C IV are also resonant lines. Further, the S IV and N IV lines are rather faint or not detected in the UV spectra of J104457 and J141851, and thus, only the O III] and O IV] lines, along with He II, since its velocity profile shows the emission is mostly nebular in origin, remain to robustly constrain our models. Therefore, in order to expand our suite of strong UV emission lines constraining the shape of the ionizing continuum, we also consider the low-resolution HST/COS G140L spectra for these galaxies, which provide access to the C III]  $\lambda\lambda$ 1907,1909 lines.

The NUV acquisition images, whose flux is dominated by the light from the young ionizing stellar clusters, are shown in the left panels of Figure 1, and highlight the simple, very compact nature of these galaxies. The UV light from J104457 and J141851 is easily contained within the COS 2."5 aperture (gold circle), corresponding to a physical size of  $\leq 0.5$  kpc at

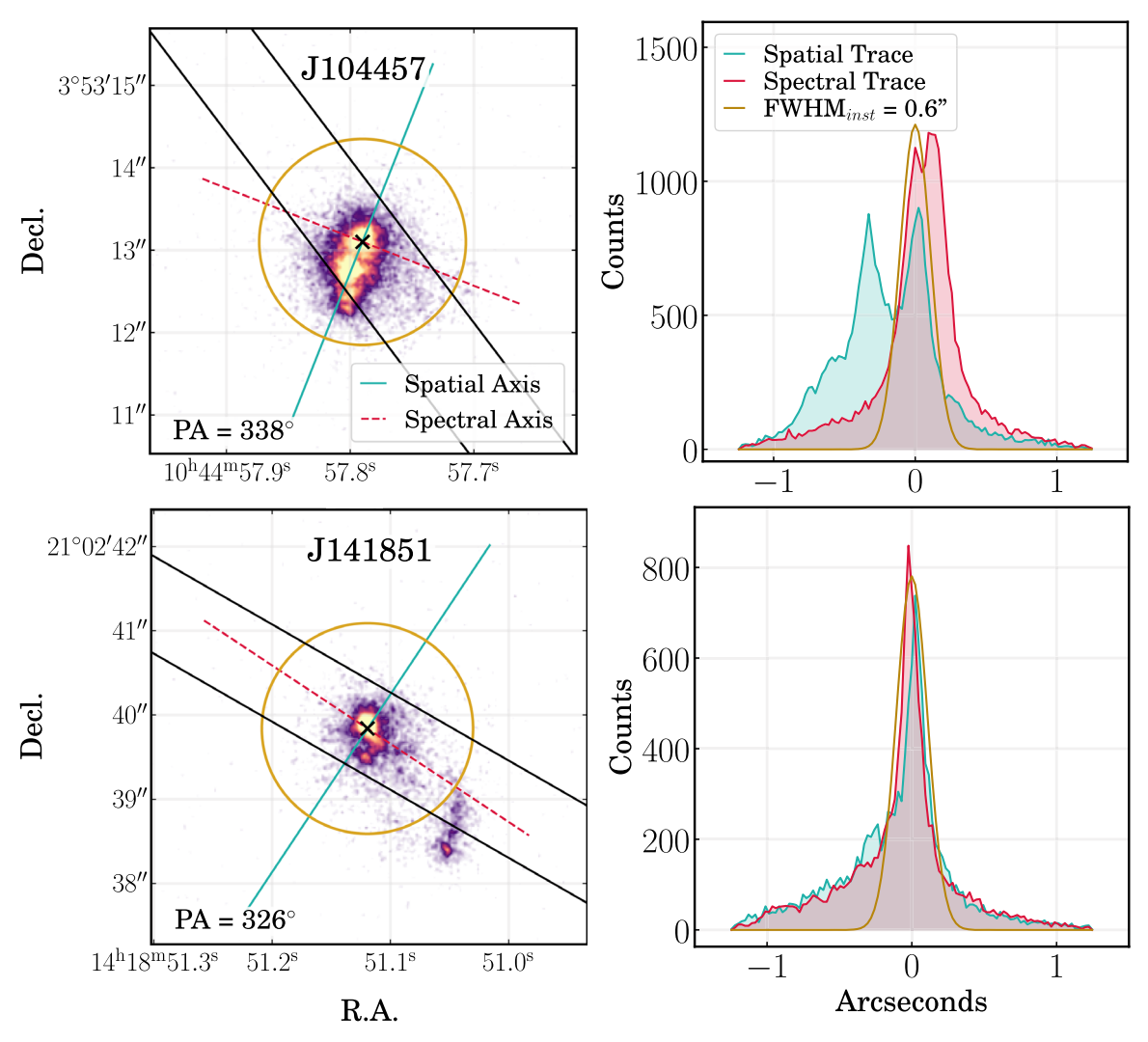


**Figure 1.** The HST/COS NUV acquisition images of J104457 (top) and J141851 (bottom) are shown in the left column. The 2."5 COS aperture used for the UV spectra is shown as a gold circle. The spectrograph position angle is noted in the corner and is used to determine the spatial and spectral axes. In comparison, the 1" LBT/MODS slit (black lines) captures most of the NUV light, but may miss a significant fraction of the extended nebular emission. In the right column, we plot the spatial and spectral light profiles captured within the COS aperture. The 0."6 instrumental profile of COS is shown in gold.

their redshifts of  $z \sim 0.01$ . In the right panels of Figure 1, we plot the spatial light distribution perpendicular to the dispersion axis (red dashed line in acquisition images). The spatial trace is smoothed by a Gaussian 1D kernel with  $\sigma=1$  pixel and compared to a Gaussian approximation of the FWHM of the non-Gaussian instrumental profile of FWHM<sub>inst</sub> = 0."6 (gold line). Similarly, the spectral light trace is plotted in green. Comparing the observed spatial trace to the Gaussian profile estimates the spatial extent of each galaxy. J141851 has less extended emission and has a fitted FWHM = 0."12. However, the spatial profile of J104457 is somewhat larger (FWHM = 0."7), resulting in a degradation of the spectral resolution.

We measured the resolution of our spectral observations by fitting Gaussian profiles to three Milky Way absorption lines in the spectra of each galaxy (Si II  $\lambda1526,$  C IV  $\lambda\lambda1548,1550,$  and Al II  $\lambda1671).$  For each galaxy, we averaged the FWHM of the three lines together to find the spectral resolution. For J104457 and J141851, we found that the FWHM related to the spectral resolution was 188 km s $^{-1}$  and 104 km s $^{-1}$ , respectively, which we reported in Table 1. These values are larger than the native

COS resolution: nominally, the spectral resolution for the G160M grating is  $R \sim 20$ , 000 or  $\Delta v = 15$  km s<sup>-1</sup>, with the observed spectral resolution broadened due to the considerable spatial extent of the galaxies (Figure 1). Similarly, Berg et al. (2019b) reported FWHMs of the O III] nebular emission lines of  $\Delta v = 87.3$ , 64.7 km s<sup>-1</sup> for J104457 and J141851, respectively (Berg et al. 2019b). Some of this velocity width could be due to the physical properties of the gas, but a degradation of the spectral resolution is also present. Nonetheless, at these resolutions, the individual emission line fluxes and velocities of interest can be resolved and precisely measured.

## 2.2. Optical LBT/MODS Spectra

While the FUV spectra enable modeling of the massive star populations, the FUV contains a limited number of nebular emission lines of only a handful of ions. Recently, Paper I presented a more detailed examination of the extreme emission lines in J104457 and J141851 and their chemical abundances, using the HST/COS G160M spectra together with new optical spectra from the Multi-Object Double Spectrographs (MODS;

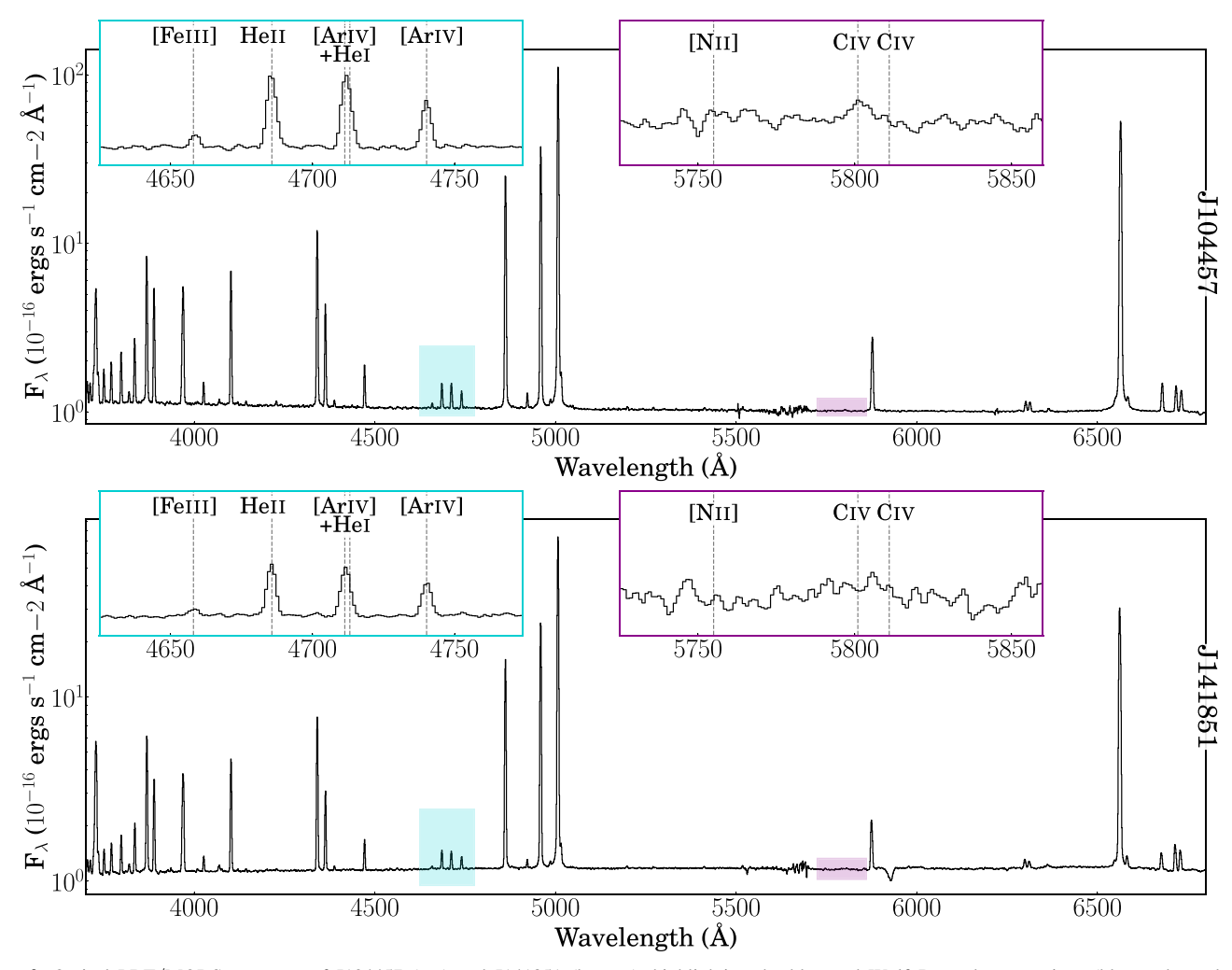


**Figure 2.** Optical LBT/MODS spectrum of J104457 (top) and J141851 (bottom), highlighting the blue and Wolf–Rayet bump regions (blue and purple inset windows, respectively). In the blue inset window, there are strong emission lines, but they appear narrow and nebular in origin, whereas there is a lack of any features in the purple inset window for J141851 but a possible C IV bump in J104457, which we discuss in Section 5.3. (The data used to create this figure are available.)

Pogge et al. 2010) on the Large Binocular Telescope (LBT; Hill et al. 2010). We refer the reader to Paper I for a full description of the observations and Berg et al. (2015) for a detailed discussion of the MODS data reduction pipeline. For convenience, we present a brief overview below.

MODS optical spectra of J104457 and J141851 were obtained on the UT dates of 2018 May 19 and 18, respectively. We obtained simultaneous, moderate-resolution blue ( $R \sim 1850$ ) and red ( $R \sim 2300$ ) spectra. J104457 and J141851 were each observed using the 1" longslit for 45 min. Spectra were reduced with the MODS reduction pipeline. One-dimensional spectra were corrected for atmospheric extinction and flux calibrated based on observations of flux standard stars (Oke 1990). A portion of the resulting spectra are plotted in Figure 2, showing the broad spectral coverage provided by this LBT/MODS setup, extending from 3200–10,000 Å and including a number of very-high-ionization emission lines: [Ne III]  $\lambda 3869$ , [Fe V]  $\lambda 4227$ , He II  $\lambda 4686$ , and [Ar IV]  $\lambda \lambda 4711,4740$ . While only the

UV spectra can be used to determine the massive star populations, we can use the high-ionization UV and optical emission lines together to better constrain the shape of the ionizing spectral energy distribution (SED).

## 3. The Stellar Continuum

## 3.1. Fitting the UV Continuum

We use the fitting procedure introduced in Chisholm et al. (2019) to determine the properties of the stellar populations in these galaxies. We first mask out any features in the spectrum that are produced by nonstellar sources. For example, lines produced by Milky Way absorption and interstellar medium emission and absorption lines associated with the galaxies are masked. We used Leitherer et al. (2011) and Bruhweiler et al. (1981) as references to identify the lines to mask. In addition to masking the spectral lines not associated with the stars, we masked the regions of the spectrum where  $\mathrm{S/N} < 1$ . These masked regions are shown as the gray bands in Figure 3. We also normalize the spectrum by the flux density at 1495 Å in order to do our fitting.

<sup>6</sup> http://www.astronomy.ohio-state.edu/MODS/Software/modsIDL/

At the spectral resolution of the LBT/MODS spectra, we observe [Ar IV]  $\lambda$ 4711+He I  $\lambda$ 4713 as a blended line profile. Therefore, the predicted He I  $\lambda$ 4713 flux is subtracted to determine the residual [Ar IV]  $\lambda$ 4711 flux.

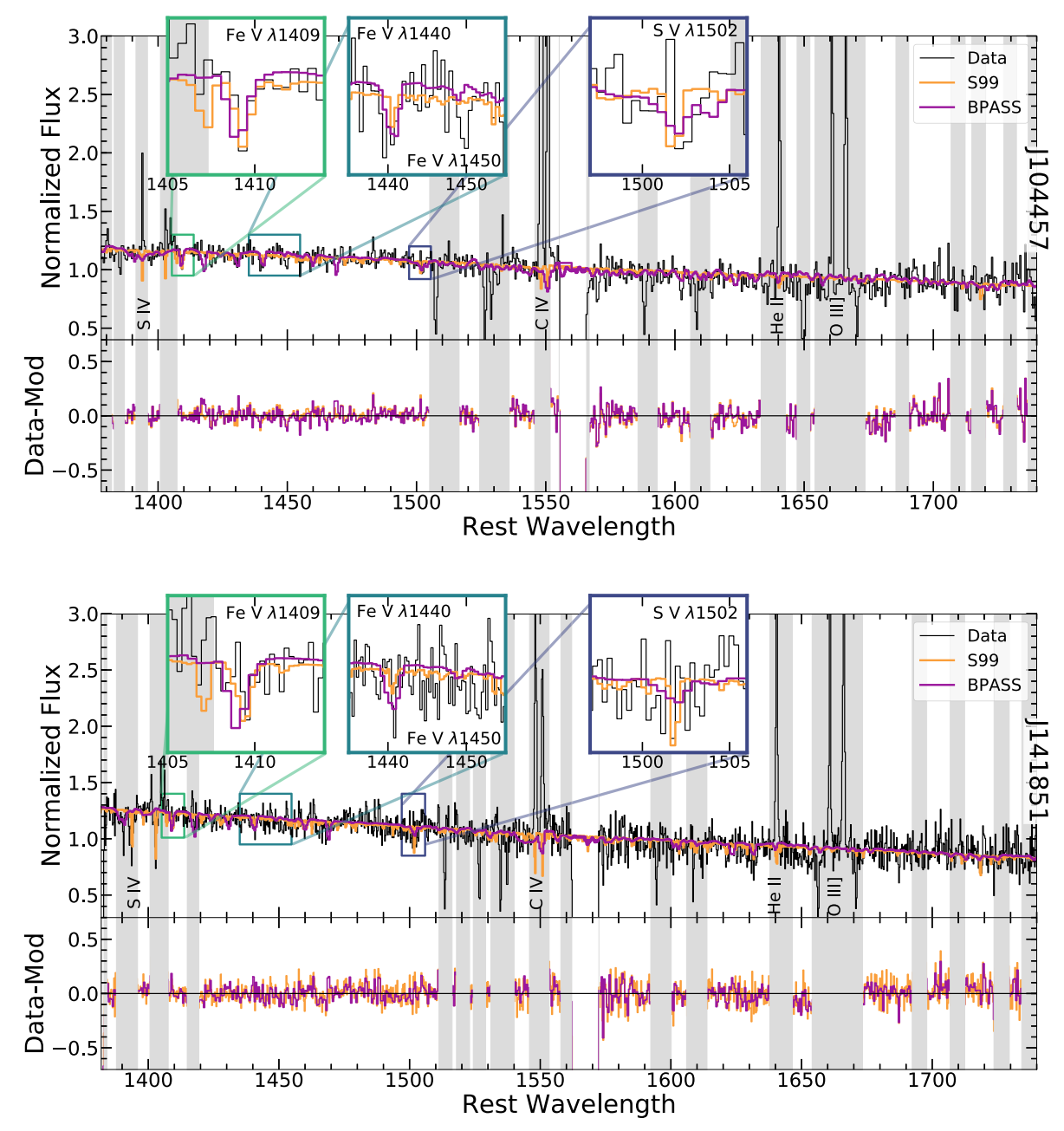


**Figure 3.** The UV spectra of J104457 and J141851 and the best-fit continuum models. The data are plotted in black, and the spectra are normalized by their flux at 1495 Å. We show the continuum fits from the Starburst 99 models (Leitherer et al. 1999) in orange and BPASS models (Eldridge et al. 2017) in pink for J104457 in the top panel and J141851 in the bottom panel. We also plot the residuals, continuum fit subtracted from the data, in the bottom plot of each panel. The zoomed-in regions highlight detections of absorption lines from highly ionized metal absorption features—Fe V and S V—that are only present in the photospheres of the most-massive and hottest stars.

To obtain the age and metallicity of the stellar populations, we compare the spectra to theoretical models of single-age bursts of star formation. We test single-star evolution using the high massloss rate stellar evolution models (Meynet et al. 1994) from Starburst99 (S99; Leitherer et al. 1999) and binary stars from BPASS v2.2.1 (Eldridge et al. 2017; Stanway & Eldridge 2018) separately. We explore Kroupa initial mass functions (IMFs; Kroupa 2002) with a broken power law with high- and low-mass slopes of 2.3 and 1.3, respectively, and both  $100~M_{\odot}$  and  $300~M_{\odot}$  high-mass cutoffs. Our model grids for both single stars and binary stars cover a range of metallicities from  $0.05~Z_{\odot}$  to  $2~Z_{\odot}$  (0.05, 0.2, 0.4, 1.0, and  $2.0~Z_{\odot}$ ) and ages from 1–15 Myr in eight nonuniform steps (1, 2, 3, 4, 5, 8, 10, and 15 Myr) selected to

capture variations in the FUV stellar continuum features with age. We used these ranges of metallicities and ages because these galaxies appear to be young, metal-poor star-forming objects based on their extreme  $H\beta$  EWs and high star formation rates (SFRs; Berg et al. 2016, 2019a). We do not expect, nor do we find, that high metallicity or old stellar populations create the observed UV spectrum as it is dominated by the light from the most-massive stars from young stellar populations, but we included the models to ensure we did not introduce this bias to our fitting method.

We convolve the 0.4 Å resolution of the S99 single-star models to the spectral resolution of the individual galaxy spectra (Meynet et al. 1994; Leitherer et al. 1999). For the

 Table 1

 Extreme UV Emission-line Galaxy Properties

Property	Units	J104457	J141851
	Adopted from	n Archival Sources:	
Reference		B16	B19b
RA		10:44:57.79	14:18:51.13
Dec		+03:53:13.15	+21:02:39.74
z		0.013	0.009
$\log M_{\star}$	$M_{\odot}$	6.80	6.63
log SFR	$M_{\odot} { m yr}^{-1}$	-0.85	-1.16
log sSFR	$ m yr^{-1}$	-7.64	-7.79
E(B-V)	mag.	0.077	0.140
$12 + \log(O/H)$	$\operatorname{dex} (Z_{\odot})$	7.45 (0.058)	7.54 (0.071)
$\log U$		-1.77	-2.42
D	erived from the U	JV COS G160M Spect	tra:
EWOIII	Å	-2.89, -6.17	-1.68, -4.78
$EW_{CIV}$	Å	-6.71, -2.83	-1.78, -1.43
$EW_{HeII}$	Å	-2.75	-2.82
O III] $\Delta V$	$\mathrm{km}\ \mathrm{s}^{-1}$	87.3	64.7
C IV $\Delta V$	${\rm km~s^{-1}}$	106.7, 86.2	101.8, 78.6
COS FWHM	${\rm km}~{\rm s}^{-1}$	188.4	103.5

Note. Properties of the extreme UV emission-line galaxies presented here. The top portion of the table lists properties previously reported by Berg et al. (2016) for J104457 and Berg et al. (2019a) for J141851. The R.A., decl., redshift, total stellar masses, SFRs, and sSFRs were adopted from the Sloan Digital Sky Survey (SDSS) MPA-JHU DR8 catalog (Data catalogs are available from http://www.sdss3.org/dr10/spectro/galaxy\_mpajhu.php). The Max Planck Institute for Astrophysics/John Hopkins University (MPA/JHU) SDSS database was produced by a collaboration of researchers (currently or formerly) from the MPA and the JHU. The team is made up of Stephane Charlot (IAP), Guinevere Kauffmann and Simon White (MPA), Tim Heckman (JHU), Christy Tremonti (U. Wisconsin-Madison-formerly JHU), and Jarle Brinchmann (Leiden University—formerly MPA), whereas E(B - V),  $12 + \log(O/H)$ , and ionization parameter log U were measured from the SDSS optical spectra. The bottom portion of the table lists the properties derived in Berg et al. (2019b) from the UV HST/COS G160M spectra (see Figure 2). EWs are listed for C IV  $\lambda\lambda$ 1548,1550, O III]  $\lambda\lambda$ 1661,1666, and He II  $\lambda$ 1640. We list velocity widths (FWHM),  $\Delta V$ , of O III]  $\lambda 1666$  and He II  $\lambda 1640$ , and both blue and red components of the C IV  $\lambda 1548$  profiles. Since the individual C IV lines present as doublets, we list the  $V_{\rm peak}^{\rm blue}$ ,  $V_{\rm peak}^{\rm red}$ , and  $V_{sep.}$  measured for the C IV  $\lambda 1548$  line. The final line of the table lists the spectral resolution from COS used in our continuum fitting.

binary stellar models from BPASS, the resolution is 1 Å, so our observed galaxy spectra were convolved to that larger resolution for these fits (Eldridge et al. 2017). The fitting results are shown in Section 3.2.

We fit the stellar continuum assuming that the FUV light is a linear combination of multiple single-age and single-metallicity bursts of star formation scaled by a linear coefficient. The final intrinsic stellar continuum fit is the sum of all models weighted by their coefficients. We then fit for the best-fit dust attenuation value (E(B-V)) by reddening the intrinsic spectrum using a foreground dust screen model and the Reddy et al. (2016) attenuation law. We tested using a Calzetti et al. (2000) and an SMC dust attenuation law (Gordon et al. 2003), but did not find that the continuum fits and stellar parameters, such as age and metallicity, statistically varied (although the E(B-V)) parameter changed). The final fit has 41 free parameters (40 linear coefficients for the stellar continuum models and one dust attenuation model). We derive light-weighted stellar population parameters (i.e., age and metallicity) by calculating a weighted

Table 2
Best-fit Stellar Continuum Models

		BPASS 100		BPASS 300
Model	S99 100 $M_{\odot}$	$M_{\odot}$	S99 300 $M_{\odot}$	$M_{\odot}$
J104457				
Age [Myr]	$1.04 \pm 2.75$	$4.01\pm1.13$	$1.26\pm2.36$	$4.03\pm0.85$
Metallicity $[Z_{\odot}]$	$0.09 \pm 0.05$	$0.14 \pm 0.04$	$0.08 \pm 0.05$	$0.13 \pm 0.03$
E(B-V)	$0.25 \pm 0.02$	$0.24 \pm 0.02$	$0.21\pm0.02$	$0.26\pm0.02$
$\begin{array}{c} \log(\xi_{\rm ion}) \\ [{\rm phot~Hz} \\ {\rm erg}^{-1}] \end{array}$	$25.9 \pm 0.9$	$25.7 \pm 0.8$	$25.9 \pm 0.8$	$25.8 \pm 0.8$
J141851				
Age [Myr]	$10.59 \pm 6.41$	$3.37\pm1.24$	$9.69 \pm 6.62$	$4.56\pm1.08$
Metallicity $[Z_{\odot}]$	$0.06\pm0.05$	$0.06 \pm 0.04$	$0.08 \pm 0.09$	$0.10 \pm 0.03$
E(B-V)	$0.16 \pm 0.03$	$0.17 \pm 0.03$	$0.13 \pm 0.03$	$0.16 \pm 0.03$
$\begin{array}{c} \log(\xi_{ion}) \\ [phot \ Hz \\ erg^{-1}] \end{array}$	$25.7 \pm 0.9$	$25.7 \pm 0.8$	$25.7 \pm 0.8$	$25.7 \pm 0.8$

**Note.** The stellar population parameters for the best-fit models to the UV continuum for each of the four types of models: S99  $100M_{\odot}$ —single star with  $100~M_{\odot}$  cutoff for the IMF; BPASS  $100M_{\odot}$ —binary star with  $100~M_{\odot}$  cutoff for the IMF; S99  $300M_{\odot}$ —single star with  $300~M_{\odot}$  cutoff for the IMF; and BPASS  $300M_{\odot}$ —binary star with  $300~M_{\odot}$  cutoff for the IMF. Here we report the light-weighted ages and metallicities for both galaxies. We used the Reddy et al. (2016) reddening law to determine the E(B-V). We calculated the number of ionizing photons and report them here as  $\log(\xi_{\rm ion})$ .

average using the model parameters and the best-fit linear coefficients. In Table 2, we give the light-weighted parameters as well as the ionizing photon production efficiency ( $\xi_{\text{ion}}$ ; or the production rate of ionizing photons divided by the luminosity at 1500 Å).

To find the errors on these parameters, we run the fitting code on 1000 randomized spectra. During each randomized iteration, we created the randomized spectra by multiplying the observed flux at a given wavelength by a random number with the distribution width dictated by the uncertainty on the spectrum at that wavelength. For each iteration, we estimated the lightweighted properties and then took the standard deviation of the distribution as the uncertainty on the stellar population properties.

## 3.2. Stellar Continuum Parameters

The fits to the observed stellar continua provide estimates of the massive star population of these two EELGs. The first two rows in Table 2 list the estimated light-weighted ages and metallicities of these two galaxies. We include four different sets of models that we used to fit the stellar populations: single-star evolution with a  $100 \, M_{\odot}$  upper IMF cutoff from S99 (Leitherer et al. 1999; Meynet et al. 1994), binary-star evolution with a  $100 M_{\odot}$  upper IMF cutoff from BPASS (Eldridge et al. 2017), single-star evolution with a  $300 \, M_{\odot}$  cutoff from S99 (Leitherer et al. 1999; Meynet et al. 1994), and binary-star evolution with a 300  $M_{\odot}$  upper IMF cutoff from BPASS (Eldridge et al. 2017). The fits imply that both galaxies have young ( $\lesssim$ 10 Myr) and low-metallicity (<0.15  $Z_{\odot}$ ) stellar populations. Due to the modest S/Ns, the inferred stellar population properties have relatively high errors, but the estimates using the four different model assumptions are consistent with each other within the  $1\sigma$  uncertainties. The BPASS models are not systematically older than the S99 models for these two galaxies,

likely because the fitting algorithm identified a feature corresponding to an older stellar population in J141851, pushing the S99 models to an older age.

As a measure of the total production of ionizing photons, we use the stellar continuum fits to determine production efficiency of ionizing photons ( $\xi_{\text{ion}} = Q/L_{1500}$ ) by integrating the total number of ionizing photons from the fitted stellar population model (Q) from 1–912 Å and dividing by the FUV luminosity density at 1500 Å. We find  $\log(\xi_{\text{ion}})$  values of 25.82 and 25.68 dex [photons Hz erg<sup>-1</sup>] for J104457 and J141851, respectively, with relatively large errors (0.8 dex). These values are larger than (but statistically consistent with) the  $\xi_{ion}$  values inferred from the optical H $\beta$  flux ratios (Berg et al. 2019a), suggesting that the stellar population fits are producing an approximately sufficient number of hydrogen-ionizing photons to match the observed Balmer emission lines. The total ionizing photon production is consistent regardless of the assumptions made for the stellar models (single-star versus binary-star evolution and the high-mass cutoff). Since the S99 and BPASS models produce different parameters for their age and metallicity to recreate the observed spectrum, it is surprising that  $\xi_{ion}$  is consistent between the two models (see Table 2). However, the combination of older binary stars from BPASS produces a similarly shaped ionizing continuum as the single stars combined for S99; thus, the consistency of the  $\xi_{ion}$  values is less surprising. Our high-mass cutoff models do produce  $\sim 0.1$  dex more ionizing photons in our log  $\xi_{ion}$  calculations than our  $100 M_{\odot}$  models. This difference is similar to the expected difference between the 100  $M_{\odot}$  and 300  $M_{\odot}$  models from BPASS found in Figure 35 of Eldridge et al. (2017). However, the errors on our calculated numbers are 0.8 dex, and thus the difference in the  $300 \, M_{\odot}$  and  $100 \, M_{\odot}$  models is not significant. The inclusion of the  $300 M_{\odot}$  only changes the fraction of single stars by a few percent in the BPASS models and does not imply a significant number of very massive stars (Stanway & Eldridge 2019).

## 3.3. Characteristic Stellar Spectral Features

In addition to determining the stellar populations of these galaxies, the FUV observations of EELGs present a rare opportunity to study the massive star population properties at very low metallicity ( $<10\%\ Z_{\odot}$ ). Figure 3 reveals largely featureless continua, with a very weak C IV 1550 Å wind P-Cygni wind feature observed in J141851 and a nearly flat C IV region in J104457 as can be seen in the residuals in Figure 3. These weak winds are consistent with theoretical predictions of radiatively driven stellar winds, where mass-loss rates are significantly lower at extremely low metallicity (Vink et al. 2001). While the continua are nearly featureless powerlaw spectra, at our S/N there are three identifiable weak photospheric features: Fe V 1409+1440 Å and S V 1502 Å (see Table 3; Bruhweiler et al. 1981; Leitherer et al. 2011). The combination of the weak C IV P-Cygni features, small highly ionized metal photospheric features, and an otherwise featureless stellar continuum are consistent with the young, lowmetallicity stellar populations inferred from the continuum fits.

Fe V 1409+1440 Å and S V 1502 Å absorption lines are indicative of very massive stars, as only the hottest stars keep significant amounts of Fe and S in these high of ionization states. If we observe absorption in Fe V and S V, this implies the most-massive stars are contributing most of the light for these galaxies, and the massive stars only exist as the youngest stars. In Table 3,

**Table 3** Photospheric Features

Object	Ea V (Å)	S V (Å)	Ratio
Object J104457	Fe V (Å) $0.24 \pm 0.12$	$0.12 \pm 0.11$	
J104437	$0.24 \pm 0.12$	$0.12 \pm 0.11$	≤0.52
J141851	≤0.07	≤0.10	≤1.43
$z \sim 0$			
J0021+0052	≤0.19	$0.37\pm0.21$	≥1.95
J0150+1260	$0.19 \pm 0.02$	$0.35\pm0.22$	$1.84\pm1.17$
J0808+3948	N/A	$0.38 \pm 0.09$	N/A
J0824+2806	≤0.06	N/A	N/A
J0926+4427	≤0.17	≤0.26	N/A
J0938+5428	N/A	$0.30 \pm 0.13$	N/A
J1415+0540	≤0.15	$0.47 \pm 0.16$	≥3.13
J1416+1223	€0.05	N/A	N/A
J1429+0643	≤0.21	≤0.22	N/A
J1429+1653	N/A	€0.18	N/A
COS Stack	€0.02	$0.20 \pm 0.03$	≥10.00
$z \sim 2$			
Cosmic Horseshoe	€0.26	$0.30 \pm 0.08$	≥1.15
RCS-0327-1326 Knot E	≤0.04	$0.30\pm0.06$	≥7.50
S000451.7-010321	$0.18\pm0.04$	$0.16\pm0.04$	$0.89 \pm 0.30$
S090003.3+223408	≤0.02	$0.06\pm0.03$	≥3.00
Sunburst Arc Region 5	≤0.05	$0.05\pm0.02$	≥1.00
MegaSaura Stack	≤0.01	$0.39 \pm 0.02$	≥39.00

**Note.** Table of EWs of Fe v 1440.528 Å line and S v 1501.76 Å line for our two new galaxies as well as two samples of star-forming galaxies at  $z \sim 0$  (Heckman et al. 2015; Chisholm et al. 2019) in the central section of the table and  $z \sim 2$  (Rigby et al. 2018a, 2018b) in the bottom section.

we compare the observed Fe V and S V EWs of our two EELGS to two samples of star-forming galaxies at  $z \sim 0$  (Heckman et al. 2015; Chisholm et al. 2019) and  $z \sim 2$  (Rigby et al. 2018a, 2018b), as well as the stacked composites for both samples (bottom of each section). The S V EWs of both galaxies are significantly weaker than the comparison samples, likely because the metallicities of the EELGS are a factor of 5-10 lower than the comparison samples. Interestingly, the Fe V 1440 Å detection in J104457 is among the strongest detections in the sample. While these two EELGS have low Fe-abundances (Paper I), the Fe V feature is actually stronger than the alpha-element tracer S V. This suggests that the iron opacity within the atmospheres of these low-metallicity stars is nonnegligible. The only other spectra with Fe V 1440 Å strongly detected are J0150+1260, which is the galaxy with the secondyoungest starburst in the Chisholm et al. (2019) low-redshift sample at  $2.20 \pm 2.17$  Myr, and S000451.7-010321, which is dominated by a very young stellar population with a small contribution from an older population, suggesting that Fe V 1440 Å is a robust indicator of very young stellar populations even at low metallicity. This is consistent with the slightly older stellar population fit to J141851 and the nondetection of Fe V 1440 Å. These detections of Fe and S photospheric lines suggest that the UV dominant stars in these two EELGS are extremely young, massive, and low-metallicity.

# 4. Photoionization Modeling

# 4.1. Adopted Nebular Property Constraints

Owing to the detection of a number of very-high-ionization emission lines (e.g., C IV, He II, O IV], Si IV, [Ne V], and [Ar IV]), we adopted a novel four-zone ionization model in Paper I and recalculated the nebular properties and chemical

abundances of J104457 and J141851. Therefore, for consistency, we adopt the results of Paper I as a better estimate of the nebular properties of J104457 and J141851 in our photoionization models. Here we briefly discuss the nebular properties that we use to constrain the shape of the ionizing SEDs of EELGs.

## 4.1.1. Suite of UV+Optical Nebular Emission Lines

In order to compare our observations to photoionization modeling, we first need to precisely measure a suite of UV and optical emission lines that probe a large range in ionization potential energy. We began by adopting the nebular emission line intensities measured in Paper I. The detailed information on the line measurement and dereddening processes can be found in Section 2.3 of Paper I and the subsequent emission line intensities in their corresponding Table 2. To briefly summarize, the UV and optical emission lines were measured in a uniform, consistent manner. The optical emission lines were measured from continuum-subtracted LBT/MODS spectra using Gaussian profile fits. The UV emission lines, on the other hand, were measured prior to continuum subtraction (as the UV continuum was not yet fit at the time of writing of Paper I) and so used a local linear continuum fit and Gaussian emission profile. Both UV and optical emission lines were corrected for Galactic extinction using the Green et al. (2015) extinction map with a Cardelli et al. (1989) reddening law, followed by an internal reddening correction determined from the Balmer decrement and the Cardelli et al. (1989)/Reddy et al. (2016) reddening law for the optical/UV lines. As the UV and optical emission lines were measured with different apertures, we scaled the UV lines to match the optical lines by measuring the UV emission lines with respect to the O III]  $\lambda\lambda$ 1661,1666 and then scaled them by the theoretical ratio of O III]  $\lambda\lambda$ 1661,1666 to [O III]  $\lambda$ 5007. We note that this ratio is temperature sensitive, so we used the temperatures we measured in Paper I to determine the theoretical ratios. To finish the scaling process, we divide the newly scaled UV line measurements by the  $[O III]/H\beta$  measurements for each galaxy. We applied this scaling to all of the UV emission lines we used. The aperture differences are small due to the compact nature of the high-energy emission lines, as shown in Berg et al. (2019a). A fuller explanation of the aperture differences is presented in Section 2.4 of Paper I. The aperture differences cause <5% differences in the relative fluxes when compared between the MODS spectra and the Sloan Digital Sky Survey (SDSS) spectra, which were measured with a similar aperture as the COS observations.

The suite of emission line measurements we adopt for comparison with our photoionization modeling is reproduced in Table 4. Specifically, we focus on the following emission lines for different ionization zones:

- 1. Low-ionization zone: [O II]  $\lambda\lambda7320,7330$ , [N II]  $\lambda6584$ .
- 2. Intermediate-ionization zone: [Ar III]  $\lambda$ 7136, [S III]  $\lambda$ 6312.
- 3. High-ionization zone: O III]  $\lambda\lambda$ 1661,1666, [O III]  $\lambda$ 5007, [Ar IV]  $\lambda\lambda$ 4711,4740, [Ne III]  $\lambda$ 3869.
- 4. Very-high-ionization zone: O IV]  $\lambda\lambda 1401,1405,1407$ , C IV  $\lambda\lambda 1548,1550$ , He II  $\lambda 1640$ ,  $\lambda 4686$ .

We based the ionization zone energy limits on specific emission line energy ranges: low-ionization is based around the [N II] line, intermediate-ionization energies are based on the [S III] line, the high-ionization energies follow the [O III] line, and the very-high-ionization energies are based on He II.

**Table 4** Ionization Line Suite

Ionization Zone	Energy (eV)	Species	Wavelength [(Å)
Low	14–29	[N II]	6584
(14–29 eV)	13–35	[O II]	7320, 7330
Intermediate	24–35	[S III]	6312
(24–35 eV)	27–41	[Ar III]	7136
High	35–55	[O III]	5007
(35-55 eV)	41–60	[Ar IV]	4740
	41–63	[Ne III]	3869
Very High	>54	He II	1640
(>54 eV)	>54	Не ІІ	4686
	55–77	O IV]	1401, 1407

**Note.** The suite of ionization lines we use in this work to test the fit between the photoionization models and the observations.

Our choice of emission lines is strategic to cover the expanse of energy ranges possible for emission lines. There are higher-energy emission lines measured in Paper I including [Fe V] and [Ne V]. We do not include these emission lines in our initial fitting due to variations in measuring the iron abundance in these galaxies and uncertain continuum measurements in the wavelength range around [Ne V]. Additionally, we use the [O II]  $\lambda\lambda7320,7330$  instead of the [O II]  $\lambda\lambda3727,3729$ , as they are not density sensitive.

#### 4.1.2. Ionization Structure

In Paper I, we used the suite of nebular emission lines to measure the ionization parameter  $\log U$  for these two EELGs and found that the ionization structure is not well described by a single  $\log U$  measurement from  $[O\ III]/[O\ II]$ . Classically, studies use three ionization zones to describe the ionization structure of a galaxy or an H II region. Using the four-zone ionization model, we were able to constrain the  $\log U$  for three ionization zones of the nebula to better understand the high-, intermediate-, and low-ionization-energy photons separately. As a result, we adopted these three ionization parameters from Table 3 of Paper I for comparison with our photoionization modeling.

#### 4.2. Photoionization Modeling

The richness and quality of our combined UV and optical spectra of J104457 and J141851 allowed us to perform the first detailed models of these spectra with the goal of simultaneously constraining the direct-method gas-phase properties, inferred ionizing stellar populations, and the resulting nebular emission lines they produce. To do so, we used CLOUDY version C17.01 (Ferland et al. 2017) to run spherical models with radiation field inputs from (1) single-aged bursts of binary-star formation from the BPASS 2.2 models (Eldridge et al. 2017; Stanway & Eldridge 2018) in Section 4.2.1, (2) the stellar population continuum fits from Section 3 in Section 4.2.2, and (3) combination models of the fitted stellar populations plus an extra high-energy source modeled as a blackbody in Section 4.2.3 in order to recreate our very-high-energy ionization lines.

#### 4.2.1. Single-aged Burst Binary Models

For our fiducial model grid, we used BPASS binary, singleaged stellar population models with ages ranging from 1-10 Myr and spanning a metallicity range of 0.005  $Z_{\odot} < Z < 0.3$   $Z_{\odot}$ (Eldridge et al. 2017; Stanway & Eldridge 2018). We matched the gas-phase metallicity to the stellar metallicity in the models, as expected for alpha-elements, but investigated subsolar abundance patterns of carbon and nitrogen relative to oxygen following the empirical trends seen for metal-poor dwarf galaxies (e.g., van Zee & Haynes 2006; Berg et al. 2012, 2019b). Paper I investigated the possibility of enhanced  $\alpha$ /Fe ratios in our EELGs but found no evidence that the inclusion of increased  $\alpha$ elements was capable of producing the high-energy photons that are missing from these galaxies. Specifically, we varied the fraction of C/O and N/O relative to solar from 0 to 1 in steps of 0.25, encompassing the measured abundances of N/O = 0.44 $N/O_{\odot}$  and  $0.32 N/O_{\odot}$  and  $C/O = 0.42 C/O_{\odot}$  and  $0.35 C/O_{\odot}$ for J104457 and J141851, respectively. We fixed the values of Ne/O, S/O, and Ar/O to solar since the abundances measured by Paper I are consistent with the solar values measured in Asplund et al. (2009). We also fix Fe/O at solar for the main models since we are not using iron lines for comparison; however, we adjust the abundance to the subsolar values measured in Paper I in Appendix B where we include iron lines in our comparisons. Finally, we used a variety of constant densities ranging from  $10-10,000~{\rm cm}^{-3}$  in logarithmic steps. We also used power-law density gradients of the form  $n(r) = n_0(r_0)(r/r_0)^{\alpha}$ , where  $n_0$  is the density at the illuminated surface of the cloud, which we set to 10 cm<sup>-3</sup>, 100 cm<sup>-3</sup>, 1000 cm<sup>-3</sup>, and 10,000 cm<sup>-3</sup>, and where  $r_0$  is the radius from the source to the illuminated surface of the cloud, and slopes of  $\alpha = [-1, -2, -3].$ 

We compare our models to the observed spectra of J104457 and J141851 by comparing the emission line ratios of different species. For our study, we use eight emission lines from the optical spectrum relative to H $\beta$ : [O II]  $\lambda\lambda7320,7330$ , [N II]  $\lambda$ 6584, [Ar III]  $\lambda$ 7136, [S III]  $\lambda$ 6312, [O III]  $\lambda$ 5007, [Ar IV]  $\lambda\lambda4711,4740$ , [Ne III]  $\lambda3869$ , and He II  $\lambda4686$ ; and two UV lines relative to O III]  $\lambda 1666$ : He II  $\lambda 1640$  and O IV]  $\lambda\lambda 1401,1407$ . We use these lines from the optical spectrum to cover emission lines produced by ionization zones from lowto very-high-ionization and are not highly temperature and density dependent, except for [O II]  $\lambda\lambda7320,7330$ , which is temperature sensitive but not density sensitive. We use [OII]  $\lambda\lambda7320,7330$  because we are using O III] and O IV] (Berg et al. 2015). We only use the He II and O IV lines from the UV spectrum because the only other available lines are CIII] and C IV, which we do not use because of inconsistencies in the C/Oabundance measurement, which are described in Section 5.2.

Similar to Berg et al. (2018) and others, we start by first finding the best-fit model from our fiducial grid by using a reduced- $\chi^2$ ,  $\chi^2_{\rm red}$  fit. We compare the line ratios of low-ionization-energy species from J104457 and J141851 and the sample of small star-forming galaxies presented in Berg et al. (2019b) to these single-age bursts and find good agreement with the models. Specifically, our models fit [N II], [O II], [S III], and [Ar III] well. In the top row of Figure 4 we have plotted the BPASS single-age burst models from 1 Myr (solid lines) to 3 Myr (dashed lines) for metallicities ranging from 0.005–0.3  $Z_{\odot}$ . The points for each galaxy are color-coded by their metallicity. The results of the reduced  $\chi^2$  of each fit ( $\chi^2_{\rm red} = \chi^2/{\rm d.o.f.}$ ), the log U, the metallicity, the age, the C/O,

and the N/O ratios are listed in Tables 5 and 6 for J104457 and J141851, respectively. Although these models fit the low- and intermediate-ionization lines relatively well (the lines with ionization energies up through [Ar III]), the  $\chi^2_{\rm red}$  is very large for the high- and very-high-ionization lines (lines with ionization energies for [O III] and >35 eV). The single-burst models do not match the high-ionization emission lines.

When we compare the high- and very-high-ionization-energy line ratios (O III], [Ar IV], [Ne III], He II  $\lambda$ 4686, He II  $\lambda$ 1640, and O IV]) predicted by the single-age burst models to the observed ratios from J104457, J141851, and the Berg et al. (2019b) sample, we find an offset in the line ratios. The observed high-ionization lines are systematically higher than the ratios predicted by the single-age bursts. We attempted changing a number of additional parameters in our models including ionization parameter, density, and power-law density distributions in order to recreate the observations, but these changes were still not enough to reproduce the observed line ratios. We show this offset in the lower panels of Figure 4. We conclude that single-age bursts of star formation as predicted by BPASS do not produce enough high-energy photons to recreate the observed highly ionized gas.

## 4.2.2. Stellar Population Fit Models

The single-age bursts of star formation underpredict the high-energy ionization lines as shown in Section 4.2.1. We have more knowledge of the stellar populations in J104457 and J141851 than most EELGs, because we have observations of the FUV stellar continuum, which we fit in Section 3. As a result, we can test whether the observed stars are capable of producing the high-energy ionization lines by using the ionizing spectrum from the stellar populations discussed in Section 3.2 as the input for our CLOUDY models. We fix our stellar parameters to those produced in Section 3.2 for these models, but we vary the gas-phase parameters to match the nebular properties of 104557 and J141851 published in Paper I. Just as was done for the fiducial models, both constant density and power-law density distributions were considered. The effects of a power-law density distribution are negligible for reproducing high-ionization emission, and thus we only present the results from our constant density models.

We also specialized our fits for J104457 and J141851 by adjusting the C/O and N/O ratios to the values reported in Paper I to see if these models would reproduce the high-ionization lines we observed. Again, we fixed the Ne/O, Ar/O, and S/O to Asplund et al. (2009) values as the values measured in Paper I are consistent with solar. We set the metallicity of the gas to the metallicity measured in Paper I and then varied the metallicity with linear steps of 0.02 (2%  $Z_{\odot}$ ). The results of these models can be seen in the first (J104457) and third (J141851) columns of Figure 5. We plot the metallicity steps around the observed metallicity as colorful lines and the observed metallicity as the black line for each galaxy. The additional five emission lines that we used in these fits are shown in similar plots in the figure in Appendix A.

As we did with the models in Section 4.2.1, we fit the models to the observed line ratios from the eight optical lines shown in Figure 4 and the two UV lines. These results are shown in the Section 4.2.2 region of Tables 5 and 6. Similar to the models from the previous section, the models that are specialized using the observed stellar population and gas-phase abundances do a reasonable job of reproducing the low- and

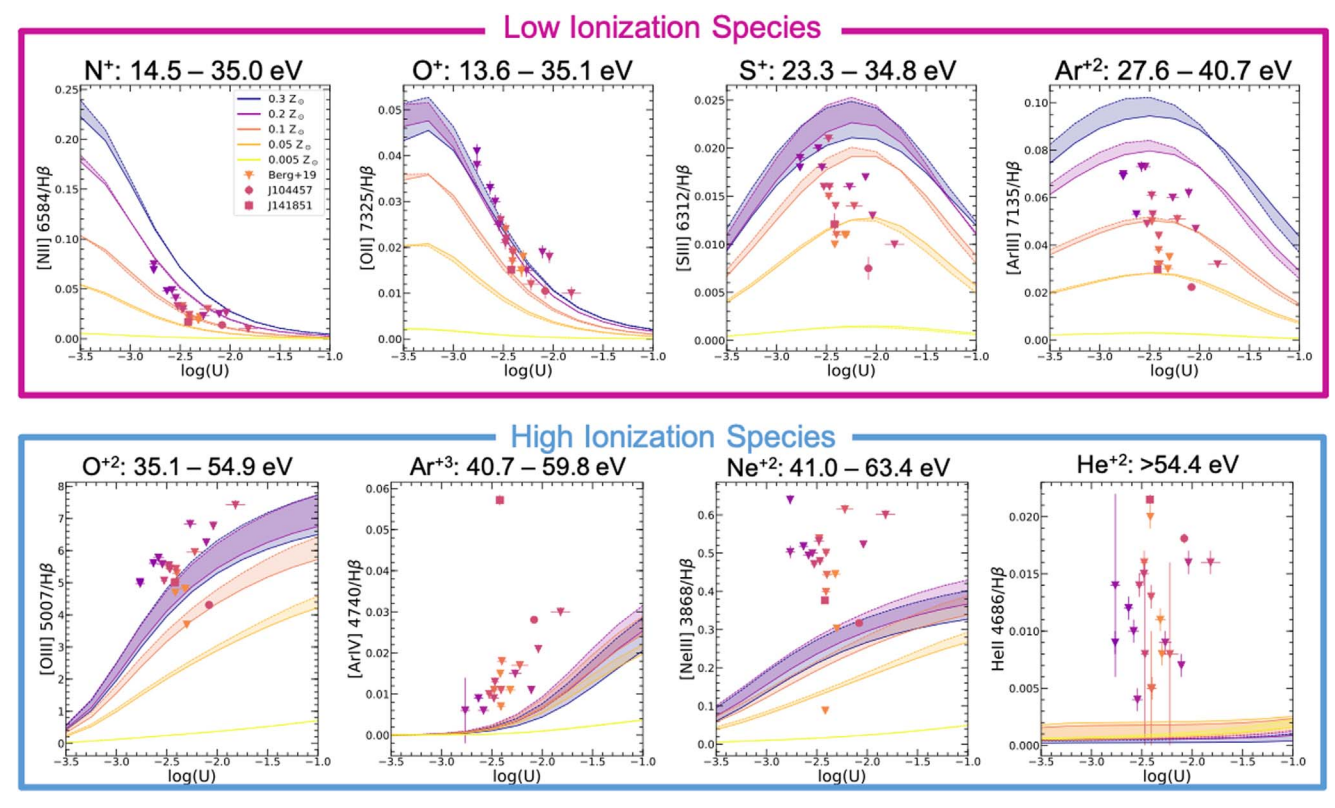


Figure 4. CLOUDY photoionization models of several nebular emission line ratios resulting from BPASS single-age stellar populations. The models are color-coded by their metallicity and are plotted as shaded bands to represent the range of ages, with the lower edge at 1 Myr and the upper edge at 3 Myr. For comparison, we plot the observed line ratios from J104457 (circular point), J141851 (square point), and the Berg et al. (2019b) sample (triangular point). The points are color-coded according to the measured nebular metallicity of each galaxy, along the same color scale as the models. The line ratios plotted are separated by their ionization potential energies such that low-ionization species are in the top row, and high-ionization species are in the bottom row, demonstrating the progressive discrepancy between models and observations with higher ionization potential.

**Table 5** J104457 Fit Parameters

Model	Ionization Zone	J $104457 = 0.058~Z_{\odot}$							
Section	and (Lines Used)	$\chi^2$	$\log U$	$Z(Z_{\odot})$	Age (Myr)	$\frac{C/O}{(C/O)_{\odot}}$	$\frac{N/O}{(N/O)_{\odot}}$	Temp (kK)	BB %
4.2.1	Low ([O II], [N II])	0.29	-2.5	0.05	5.01	0.25	0.25	•••	
Single-aged Burst	Inter. ([S III], [Ar III])	0.71	-3.0	0.05	10.0	1.25	1.25		
Binary Models	High ([O III], [Ar IV], [Ne III])	34.52	-1.0	0.05	1.0	0.25	0.25		
	V. High (He II,He II,O IV])	391.49	-1.0	0.15	3.16	0.25	0.25		•••
	All 10	151.14	-1.0	0.15	3.16	1.25	1.25	•••	
4.2.2	Low ([O II],[N II])	2.03	-2.5	0.05	4.01	0.34	0.32		
Stellar Population	Inter. ([S III],[Ar III])	1.14	-3.25	0.05	4.01	0.34	0.32		
Fit Models	High ([O III],[Ar IV],[Ne III])	35.19	-2.0	0.11	4.01	0.34	0.32	•••	
	V. High (He II,He II,O IV])	479.40	-1.0	0.01	4.01	0.34	0.32		
	All 10	174.10	-1.75	0.07	4.01	0.34	0.32	•••	•••
4.2.3	Low ([O II],[N II])	1.90	-2.25	0.058	4.01	0.34	0.32	60	75
Combination Stellar +	Inter. ([S III],[Ar III])	2.94	-3.5	0.058	4.01	0.34	0.32	60	0
Blackbody Models	High([O III],[Ar IV],[Ne III])	58.59	-1.5	0.058	4.01	0.34	0.32	80	5
•	V. High (He II,He II,O IV])	0.88	-1.0	0.058	4.01	0.34	0.32	80	35
	All 10	30.40	-1.75	0.058	4.01	0.34	0.32	80	45

Note. J104457 parameters of best-fit stellar population and gas from models described in Section 4.2. All parameter values in *italics* denote that the parameter value was fixed for the model. In the Section 4.2.2 models the fixed parameters are the age, (C/O), and (N/O) ratios, 4.2.2 and for the Section 4.2.3 models the metallicity, age, (C/O), and (N/O) ratios were fixed. Photoionization models from Section 4.2.1 use single-age bursts of star formation from BPASS v2.1 as the input spectrum, with gas metallicities fixed to the same as the stars, but variable (C/O) and (N/O) ratios. Models from Section 4.2.2 use the ionizing continuum from Section 3.2 as the input spectrum with gas-phase metallicities varying around the gas-phase metallicity measured in Paper I, and with (C/O) and (N/O) ratios fixed to the abundances from Paper I. The models from Section 4.2.3 use the ionizing continuum from Section 3.2 plus an ad hoc blackbody as the input spectrum with fixed gas-phase metallicity and (C/O) and (N/O) ratios as measured with the four-zone abundances in Paper I.

**Table 6**J141851 Fit Parameters

Model	Ionization Zone and (Lines Used)	J141851 = $0.087~Z_{\odot}$							
Section		$\chi^2$	$\log U$	$Z(Z_{\odot})$	Age (Myr)	$\frac{C/O}{(C/O)_{\odot}}$	$\frac{N/O}{(N/O)_{\odot}}$	Temp (kK)	BB %
4.2.1	Low ([O II], [N II])	17.54	-2.25	0.1	3.16	0.25	0.25	•••	
Single-aged Burst	Inter. ([S III], [Ar III])	0.01	-1.25	0.15	5.01	0.5	0.5		
Binary Models	High ([O III], [Ar IV],[Ne III])	230.90	-1.0	0.1	1.0	0.75	0.75		
	V. High (He II,He II,O IV])	619.56	-1.0	0.15	3.16	0.25	0.25		
	All 10	315.99	-1.0	0.15	3.16	1.25	1.25	•••	
4.2.2	Low ([O II], [N II])	51.97	-2.25	0.07	3.37	0.31	0.40		
Stellar Population	Inter. ([S III], [Ar III])	1.18	-2.5	0.05	3.37	0.31	0.40		
Fit Models	High ([O III], [Ar IV], [Ne III])	19.50	-1.0	0.07	3.37	0.31	0.40		
	V. High (He II,He II,O IV])	741.94	-1.0	0.03	3.37	0.31	0.40		
	All 10	308.38	-1.75	0.11	3.37	0.31	0.40	•••	
4.2.3	Low ([O II], [N II])	68.98	-2.25	0.087	3.37	0.31	0.40	80	70
Combination Stellar +	Inter. ([S III], [Ar III])	3.81	-1.75	0.087	3.37	0.31	0.40	100	5
Blackbody Models	High([O III], [Ar IV], [Ne III])	18.32	-1.75	0.087	3.37	0.31	0.40	100	50
	V. High (He II,He II,O IV])	0.94	-2.0	0.087	3.37	0.31	0.40	80	55
	All 10	62.03	-1.75	0.087	3.37	0.31	0.40	80	55

**Note.** Same as Table 5 but for J141851. All parameter values in *italics* denote that the parameter value was fixed for the model. In the Section 4.2.2 models the age, (C/O), and (N/O) ratios 4.2.2, and for the Section 4.2.3 models the metallicity, age, (C/O), and (N/O) ratios were fixed. 4.2.3.

Table 7
Ionizing Photon Rates

	J104457	J141851
$Q_0 [s^{-1}]$	4.70 1052	1.00 1052
B19a	$4.70 \times 10^{52}$	$1.88 \times 10^{52}$
Section 3	$1.55 \times 10^{52} \ (0.33)$	$7.37 \times 10^{51} \ (0.39)$
Section 4.2.3	$3.30 \times 10^{52} \ (0.70)$	$1.85 \times 10^{52} \ (0.99)$
$Q_2 [s^{-1}]$		
B19a	$3.87 \times 10^{50}$	$1.61 \times 10^{50}$
Section 3	$8.24 \times 10^{47} \ (0.0021)$	$5.59 \times 10^{47} \ (0.0035)$
Section 4.2.3	$4.13 \times 10^{50} (1.07)$	$2.69 \times 10^{50} \ (1.67)$

**Note.** The ionizing photon rates as measured from the SDSS emission lines reported in Berg et al. (2019b), the models from Section 3, and the models from Section 4.2.3. The number in parentheses is the ionizing photon rate normalized to the measured rate from Berg et al. (2019b).

intermediate-ionization lines, but fail to reproduce the very-high-energy ionization lines. The stellar populations we observed are able to match the high-ionization lines O III] and [Ar IV] up to  $\sim\!35\,\mathrm{eV}$  that the single-age bursts could not match well, as seen in the "Stars Only" columns in Figure 5 and in the similar or lower  $\chi^2_{\mathrm{red}}$  values for the high-ionization zone for Section 4.2.2 in comparison to Section 4.2.1 in Tables 5 and 6. Although the stellar populations from Section 3.2 can recreate the low-, intermediate-, and high-ionization lines, these models are unable to produce the observed values for the very-high-ionization-energy lines like He II and O IV].

# 4.2.3. Combination Stellar + Blackbody Models

The stellar population fit models from the previous section failed to reproduce the very-high-ionization emission lines as seen in the He II and O IV] panels of "Stars Only" columns of Figure 5. This problem is often seen for He II observations (e.g., Guseva et al. 2000; Thuan & Izotov 2005; Kehrig et al. 2015, 2018, 2021;

Senchyna et al. 2017, 2020; Wofford et al. 2021), but we emphasize that the discrepancy between photoionization models using the stellar continuum as the input ionizing spectra and observations of emission lines is a problem for all very-high-energy ionization lines, especially He II and O IV], as seen in Sections 4.2.1 and 4.2.2 above. Here we explore what is required to reconcile the observed nebular emission lines with the models. In the absence of new, specialized models of low-metallicity stellar populations, we can provide a first benchmark to improve these models using the addition of a blackbody (BB).

We combine the models from Section 4.2.2 with a hot BB in order to reproduce the unexplained excess flux we observe in the very-high-ionization lines. We added BBs with temperatures of 60,000 K, 80,000 K, and 100,000 K because these temperatures span the range between the energies dominated by X-ray emission and the energies observed in the UV. Senchyna et al. (2020) demonstrated that similar objects do not have significant X-ray emission, so we avoid adding high-temperature BBs or a power-law contribution that would be detected in X-rays.

We added these three BBs (T = 60 kK, 80 kK, and 100 kK) in varying strengths by scaling the BB bolometric luminosity and adding it to the young stellar population fit such that the BB contributes roughly 5%–70% (in eight steps) of the total bolometric luminosity of the galaxy. We refer to the bolometric luminosity of the stellar population as  $L_{\rm young}$ , which we define as  $L_{\rm young} = \int_{3e12{\rm Hz}}^{3e18{\rm Hz}} F_{\nu} d\nu$  (1–100,000 Å). We define the total bolometric luminosity of the galaxies,  $L_{\rm tot}$ , as the summed bolometric luminosity of both the BB and the stellar population from Section 3,  $L_{\rm tot} = \int_{3e12{\rm Hz}}^{3e18{\rm Hz}} F_{\nu,{\rm BB}} d\nu + \int_{3e12{\rm Hz}}^{3e18{\rm Hz}} F_{\nu,{\rm stars}} d\nu$ . We add this BB to the input spectrum of the young stars and

We add this BB to the input spectrum of the young stars and then vary the  $\log U$  of the photoionization models using the combined spectra as the shape of the SED for the ionizing source.

We ran photoionization models with the same gas metallicity steps as those in Section 4.2.2; this includes the observed gasphase metallicity from Paper I and the  $2\%~Z_{\odot}$  steps around that

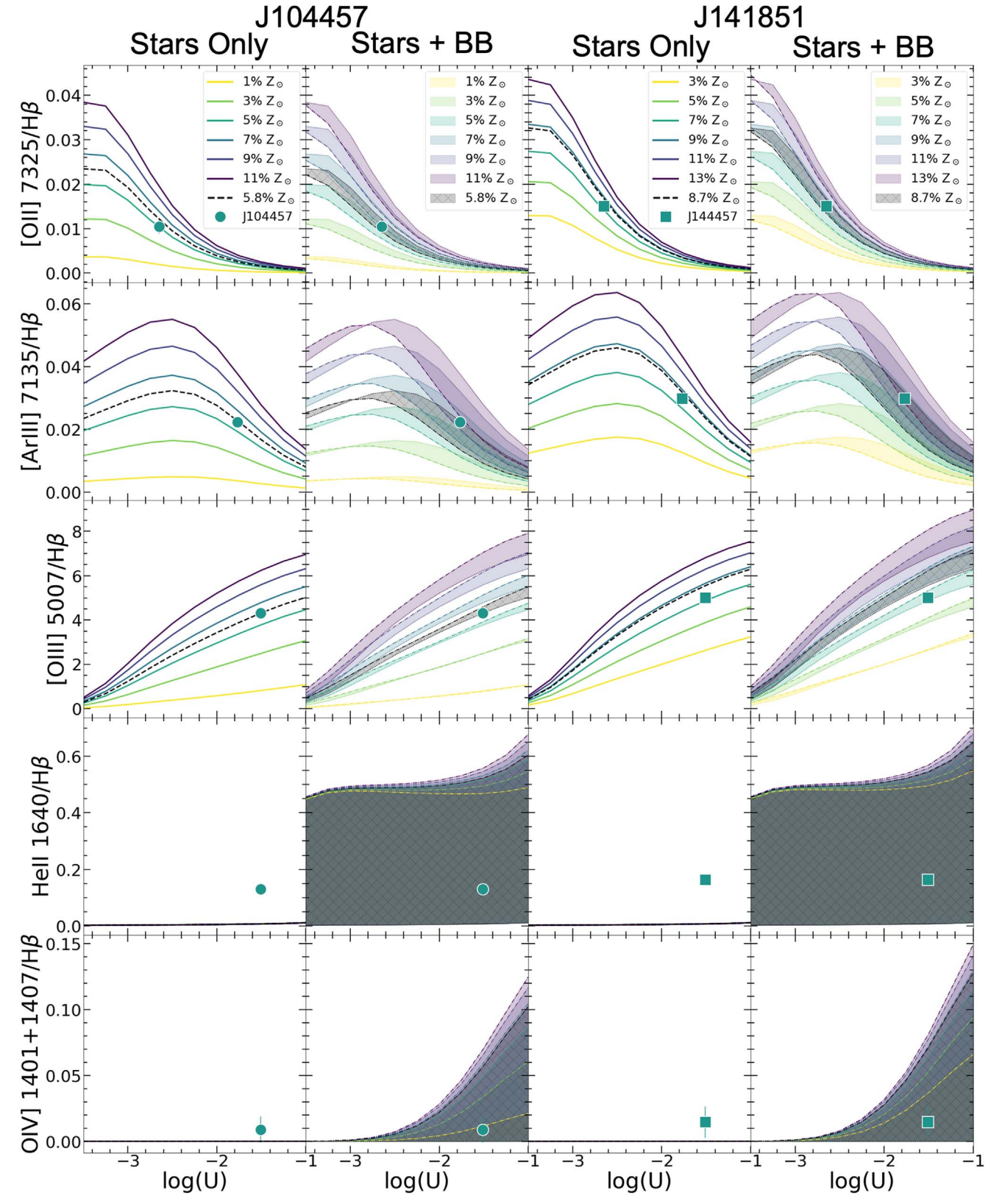
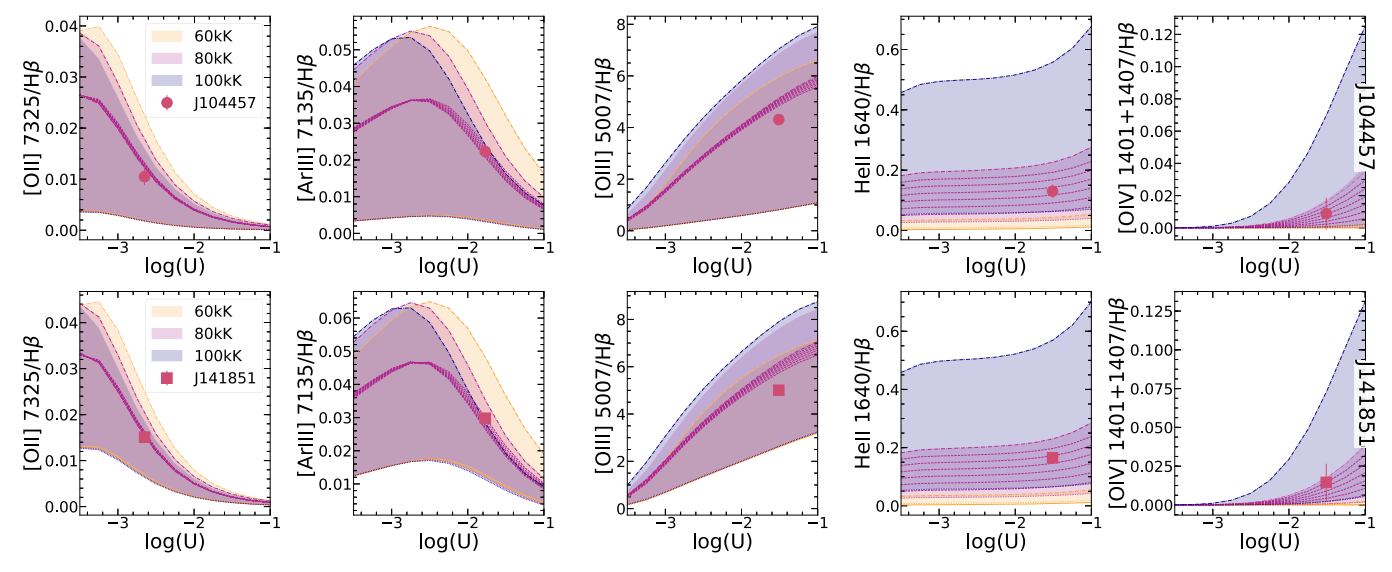


Figure 5. Line ratio diagrams for five emission lines spanning the different ionization zones with the observed line ratio plotted as the point for J104457 and J141851. The "Stars Only" column shows the CLOUDY photoionization models where we used the ionizing continuum from the stellar population we fit to these galaxies in Section 3.2 as the input ionizing spectrum. Each line is a different metallicity from low metallicity at  $1\% Z_{\odot}$  in yellow to  $11\% Z_{\odot}$  in purple for J104457, and for J141851 the range starts with  $3\% Z_{\odot}$  in yellow and goes to  $13\% Z_{\odot}$  in purple. The black dashed line shows the results of a model run with the observed gas-phase metallicity of each galaxy,  $5.8\% Z_{\odot}$  for J104457 and  $8.7\% Z_{\odot}$  for J141851. In the "Stars + BB" column, the models are plotted in bands with the same metallicity color-coding system, but the bands now include the effects of the blackbodies we modeled. The band is bordered by a dotted line showing the  $65\% L_{\text{tot}}$  from a 100 kK blackbody. The black hatched region shows the models run with the observed gas-phase metallicity of the galaxy.



**Figure 6.** Combined stellar population and BB models for J104457 and J141851 to show the effects of BB temperature and percentage. Each temperature is plotted as a different color band with 60 kK as orange, 80 kK as pink, and 100 kK as blue. The bands range from the lower dotted line as a BB with 0%  $L_{\text{tot}}$  to the upper dasheddotted line showing 75%  $L_{\text{tot}}$  and include all metallicity steps from the models. The pink dashed lines show the 10%  $L_{\text{tot}}$  steps from 5% to 75% for an 80 kK blackbody run with the observed gas-phase metallicity for each galaxy. The point is the observed line ratio for the galaxy.

measured metallicity. We used the abundances from the four-zone ionization structure as estimated by Paper I to fix our C/O, N/O, Ne/O, Ar/O, and S/O ratios.

We plot the effects of the BB on each metallicity model in the columns labeled "Stars + BB" of Figure 5. The lower bound (dashed line) of each metallicity shows the 60 kK 10% BB, while the upper bound (dotted line) plots the 100 kK 65% BB, so each band covers the entire range produced by our different BB possibilities. The black band on this plot shows the models run with the metallicity fixed at the observed metallicity. As with Section 4.2.2, the additional five emission lines that we used in these fits are shown in Figure A1 in Appendix A.

We see that the added BB increases the range of line ratios each metallicity model is capable of producing. For the observed metallicity (black band), we see that similar to the models from the previous two sections, we are still able to reproduce the emission from the low-, intermediate-, and high-ionization lines, which demonstrates that the added BB does not greatly affect the lower-energy parts of the ionizing spectrum. Additionally, the very-high-ionization lines now are included within the band the models produce. This shows us that the additional BB produces enough ionizing photons at energies >54 eV to reproduce the observed He II emission.

The shape of the BB is determined by the temperature and percent contribution to the luminosity. We show the effects of the BB temperature on the models in Figure 6: each temperature is a different color, and the shaded region spans from a lower bound of 5% BB to an upper bound of 75% BB. We plot the observed line ratios for J104457 in the top panels and J141851 in the bottom panels. The low- and intermediate-ionization lines have the ability to give us more information about the temperature of the BB. High-ionization parameters with large line ratios can rule out certain BB temperatures. The high-ionization lines provide more information about the percent contribution. The shapes of the BB models allow for any temperature to produce the very-high-emission lines. At high line ratios, higher-temperature BBs can produce the same emission with a smaller percent contribution. To demonstrate

this, we show dashed lines of each additional 10% in the percentage contribution to luminosity for the 100 kK BB. This shows that with larger percent contributions, the BB can reach increasingly extreme line ratios.

The very-high-ionization-energy lines include the most information about the BB component of the fit, as the He II and O IV] lines are most sensitive to the high-energy photons. J104457 requires an 80 kK BB with 45% of  $L_{\rm tot}$  while J141851 requires an 80 kK BB producing 55% of  $L_{\rm tot}$ . We can see for J104457 in Figure 6 that all three BB temperatures are capable of reproducing the observed line ratios for our low- and intermediate-ionization lines. For J141851 in Figure 6, we see that the [Ar III] line starts to fall outside the band of line ratios produced by the 100 kK BB, indicating a 100 kK BB may not produce the emission we see from J141851. In J104457, the low- and intermediate-ionization-energy line fits do not contain much information that constrains the BB components; but in J141851, these lines may contain some temperature information.

Our solutions employ a number of different selections of the eight optical lines and two UV lines we have been using in this paper. The fit results for J104457 and J141851 are shown in Tables 5 and 6, respectively. We report the temperature of the BB and the percentage of total light that the BB makes up in this table in addition to the columns discussed in Sections 4.2.1 and 4.2.2. The  $\chi^2_{\rm red}$  values for the combined fit from all 10 emission lines are high because the combined fits do not fit all 10 lines well simultaneously; in particular, [O III] increases our  $\chi^2_{\rm red}$  values. The combined fit does favor the BB parameter fit using only the very-high-ionization lines. This gives us confidence the BB information from all 10 lines is accurate, since the BB information matches the parameters found by the lines with the most information about the BB. When we compare the fits that include this BB to the fits from Sections 4.2.1 and 4.2.2, we see that the added BB allows for a better fit when using lines with very-high-ionization energies and in the total 10-line fit. This demonstrates that including a high-energy photon source strongly improves the predicted nebular emission structure of very-high-ionization emission line galaxies.

#### 5. Discussion

## 5.1. The High-energy Ionizing Photon Production Problem

J104457 and J141851 are two EELGs that demonstrate the inability of traditional photoionization models to accurately reproduce the very-high-energy ionization lines. We show this discrepancy in Section 4.2 with the very-high-ionization lines of He II and O IV]. In addition to the excess He II and O IV] emission we see compared to the photoionization models without an additional source of high-energy photons, J104457 and J141851 show this discrepancy in their [Fe V] emission. Paper I detailed the ionization correction factors (ICFs) for these two galaxies and found that the observed [Fe V] emission was not matched by the ICF provided from photoionization modeling, with only the observed stars producing the photons. This inability of the stellar populations to reproduce the high-energy photons through photoionization indicates there is an HEIP<sup>3</sup>, as named in Paper I.

The HEIP<sup>3</sup> is observed as excess He II emission in these two EELGs but also in the extreme He II emission observed in other blue compact dwarf galaxies (e.g., Guseva et al. 2000; Thuan & Izotov 2005; Izotov et al. 2012; Kehrig et al. 2015, 2018, 2021; Berg et al. 2018; Senchyna et al. 2017, 2020; Stanway et al. 2020). Paper I showed that the HEIP<sup>3</sup> results in underestimated ionization parameters, which, when corrected, could increase the He II emission produced by photoionization models used to compare with the extreme He II emission in blue compact dwarf galaxies. We demonstrated that even this increased ionization parameter could not account for the He II emission we observe in our two EELGs when only the stars are ionizing the gas, so it is unlikely that correcting the ionization parameter would reconcile the excess He II emission observed in other samples of blue compact dwarf galaxies or EELGs. We have found that the addition of a BB to the observationally motivated model of the stars can solve the HEIP<sup>3</sup> for J104457 and J141851. This additional source of very-highenergy photons can reproduce the very-high-ionization lines that are not reproduced as a result of the HEIP<sup>3</sup> as is described in Section 5.2.

## 5.2. Self-consistent Modeling Success

The emission lines from EELGs trace the ionizing spectrum of these galaxies, and, by using photoionization modeling, we are able to compare different forms of stellar population synthesis to the observed emission lines in order to understand what is ionizing these galaxies. We tested a number of input spectra to use in our CLOUDY photoionization modeling to reproduce the observed emission lines from these two galaxies. Using only the canonical models of single-age bursts of star formation, we were able to recreate the emission lines from low-energy ionization species, but we were unable to produce the high-energy-ionization lines with these inputs, as seen in Figure 4. Figure 4 compares emission lines from not only J104457 and J141851, but also a number of compact dwarf galaxies in the nearby universe. Notably, the models of highionization lines fall short of the observations from all galaxies we plotted. This indicates that models with a single-age burst of star formation do not produce the correct ionizing continuum shape required to reproduce the observations of EELGs.

We then tested the observed stellar populations, as we measured them from Section 3, as the input spectrum. This moved us from using sets of likely stellar populations to the

stellar population that we observed in each galaxy. These stellar populations were determined using models with and without binaries, as well as with an extended high-mass cutoff. The shapes of the ionizing continuum from the single-star and binary models were similar, so we used the binary model version, as it has better wavelength resolution over the wavelength range we used to calculate the ionizing spectrum. With this observationally motivated ionizing spectrum, we were able to reproduce the observed emission lines up to ionization energies of  $\sim$ 35 eV, like [O III], which can be seen in the "Stars Only" columns of Figure 5. The stellar model fits to the observed stars in these galaxies produce enough photons to recreate the high-energy emission lines but not the veryhigh-energy emission lines, like He II and O IV]. This inability to reproduce the highest-energy emission lines demonstrates the HEIP<sup>3</sup> as introduced in Paper I.

Since the models fit to the observed stars did not reproduce the highest-energy emission lines, we decided to add a BB to the input spectrum in order to get an idea of the temperature and percent contribution of the source needed to recreate these lines. The ad hoc BB has a peak with a temperature less than what is observable in the X-rays, because Senchyna et al. (2020) and others show that EELGs like our sample do not tend to have significant X-ray detections. The BB temperature must also be high enough to not disturb the low-energy ionization lines that are already produced by the observed stellar population. With these restrictions, we fit using eight optical lines from all four ionization zones and found that the best-fit temperature of the BB was 80,000 K, and the flux contribution for the BB was 45%-55% of the total luminosity of the combined BB and young stars,  $L_{\text{tot}}$ . Full details of the fits can be seen in Tables 5 and 6. In order to understand more about our BB, we fit the models to multiple smaller sets of emission lines. The low- and intermediate-ionization lines carry little information about the BB but do favor ionization parameters indicative of their ionization zones. In Figure 6, we see that the high- and very-high-ionization lines hold most of the information about the BB and thus determine the BB parameters for the full eight-line fit of all ionization zones. This added BB successfully reproduces the low- and intermediate-ionization lines already produced with observed stars as well as the veryhigh-energy lines that were missed.

To check the reasonableness of our fits, we compared the ionizing photons for H,  $Q_0$  and He II,  $Q_2$ . In Berg et al. (2019a), we calculated the  $Q_0$ ,  $Q_2$  from these two galaxies using the H $\beta$ and He II 4686 emission lines from the SDSS spectra. We calculated the  $Q_0$  from the models we fit in Section 3—based on the UV stellar continuum—and Section 4.2.3—based on the stellar continuum and added blackbody and reported these values in Table 7. The models for Section 3 produce lower amounts of ionizing photons in our  $Q_0$  calculations at 33% of the value calculated in Berg et al. (2019a) for J104457 and 39% of the observed value for J141851. However, they drastically underproduce the He II ionizing photons, as seen with  $Q_2$ , only 0.2% for J104457 and only 0.4% for J141851 of the measured  $Q_2$  from Berg et al. (2019b). The models from Section 4.2.3, which include the blackbody, produce similar ionizing photon counts for both  $Q_0$  and  $Q_2$ . For  $Q_0$ , these models match the measured ionizing photon rate at 70% and 99% of the measured  $Q_0$  for J104457 and J141851, respectively. For  $Q_2$ , the models only slightly overproduce (at 107% for J104457 and 167% for J141851) the measured rate in Berg et al. (2019b).

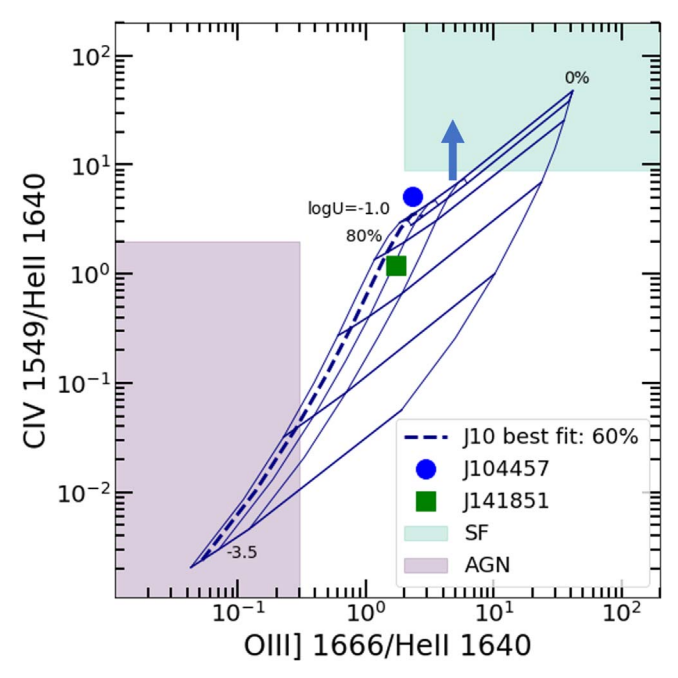


Figure 7. The UV BPT diagram plotted with C IV  $\lambda\lambda 1548,50/{\rm He~II~}\lambda 1640$  vs. O III]  $\lambda 1666/{\rm He~II~}\lambda 1640$ . The teal and purple shaded boxes highlight the regions typical of photoionization models for star formation only and AGN only, respectively. In comparison, we plot the models for J104457, where the rightmost line maps the models produced by the stellar population fits for a range of ionization parameters, extending from  $\log U = -1$  at the top to  $\log U = -3.5$  at the bottom with horizontal lines marking steps of 0.5 in  $\log U$ . Models adding contributions from an 80 kK blackbody are plotted as narrow lines, where each subsequent model to the left increases the contribution from the blackbody by 20%. The arrow indicates the direction the models should move to account for the discrepancy between abundances calculated from ICFs using continuous and burst star formation models.

This leads us to conclude that the ionizing photons of the added blackbody are reasonable in recreating the emission in these galaxies.

The idea of adding a BB to understand the ionizing radiation needed to produce the very-high-ionization lines we observe in our EELGs is not new. Steidel et al. (2014) used a similar BB to model the ionizing radiation of star-forming galaxies at  $z \sim 2-3$ , while Stasińska et al. (2015) used an additional BB to reproduce emission lines in  $z \sim 0$  galaxies in SDSS. We compare our method to previous models by plotting our models of the observed stellar population and ad hoc BB at a fixed metallicity of 0.058  $Z_{\odot}$  for J104457 as a grid on a UV diagnostic diagram as seen in Figure 7. The UV BPT diagram has been suggested as a way to determine if a galaxy is starforming or active galactic nucleus (AGN)-driven for galaxies at higher redshift where the UV diagnostic lines are the only observed diagnostics (Feltre et al. 2016). We use a diagnostic diagram consisting of C IV  $\lambda\lambda 1548,50/\text{He II}$   $\lambda 1640$  versus O III]  $\lambda 1666/\text{He II}$   $\lambda 1640$  to distinguish the star-forming and AGN-driven objects. The general range of star formation models produced in Mainali et al. (2017) is shown as the teal shaded box in the upper-right corner of the plot, while the AGN-driven models are shown in the shaded purple box in the lower left (Feltre et al. 2016). Our models are plotted as a grid, where the observed stellar population only is the rightmost line and each vertical line to the left is a 20% jump in relative flux contribution of the BB. The horizontal lines are the  $\log U$  of the model, which start at  $\log U = -1.0$  at the top, and each horizontal line is a step of 0.5 in  $\log U$  to the bottommost line of  $\log U = -3.5$ . These models move across the gap from starforming into the AGN-driven regions of parameter space, which covers the observations of these galaxies well.

The observation for J104457 lies above the model grid in Figure 7. This discrepancy between the models and the observations stems from the method for calculating the abundances based on the ICF. We used abundances calculated by Paper I who used continuous star formation models to determine the ICF for carbon in our galaxies. Continuous star formation models underpredict the ICF when compared to models with bursts of star formation, which leads to lower carbon abundances. With increased C/O values, our models would increase along the C IV  $\lambda\lambda 1548,50/\text{He II }\lambda 1640$  axis and thus encompass the observation of J104457, as indicated by the arrow in Figure 7. In similar diagnostic diagrams using C IV  $\lambda\lambda 1548.50/\text{He II }\lambda 1640 \text{ versus C III] }\lambda 1666/\text{He II }\lambda 1640, \text{ we}$ see the same effects; our models do not produce enough C emission, and by increasing the C/O abundance, our best-fit model would match the observations for these galaxies.

Our combined stellar population and ad hoc BB models span the gap between AGN- and star-formation-driven models. The space between the classical AGN and star formation models is primarily where we find EELGs like J104457 and J141851. Since local EELGs lie between AGN and star formation models, observations of high-redshift galaxies likely fall in this parameter space as well. We caution that the reality for high-redshift galaxies will not conform to only star formation or AGN models, and going forward, a composite spectrum similar to the ones developed here should be used.

In summary, the models of the observed stellar continuum are combined with an additional hot BB component in order to simultaneously fit the emission lines from all four ionization zones. This combination model reproduces the emission of He II and O IV] from the very-high-ionization zone as well as [O II] and [N II] from the low-ionization zone and lines from the zones in between. This observationally motivated stellar continuum model and ad hoc BB are capable of reproducing the emission lines from all 10 emission lines used in our fit.

## 5.3. What Is the Source of the High-energy Photons?

Our BB and observationally motivated stellar continuum combined model successfully recreates the high-energy line ratios observed in our two EELGs. The ionizing continuum of the stars, BB, and combined stars and BB are shown in Figure 8. The green line shows the ionizing continuum from the best-fit stellar population using BPASS models as described in Section 3 scaled to account for BB contribution. The black spectrum shows the observed data, while the teal line shows the BB, and the blue line shows the stars and BB combined. The circles show the intersection of each model with the wavelength required to produce He II and C IV emission and are color-coded by model.

The BBs shown in Figure 8 contribute a significant portion of the flux required to reproduce the high-energy ionization lines and create a distinctly different shape in the FUV for these galaxies. The sources(s) of the high-energy photons are, to date, unidentified. We have explored the literature and found a number of candidates that could cause the very-high-ionization emission lines we observe, and we discuss them and their feasibility below.

*Binaries.* In Section 3.2, we tested binaries in our stellar population calculation by using the BPASS models and found

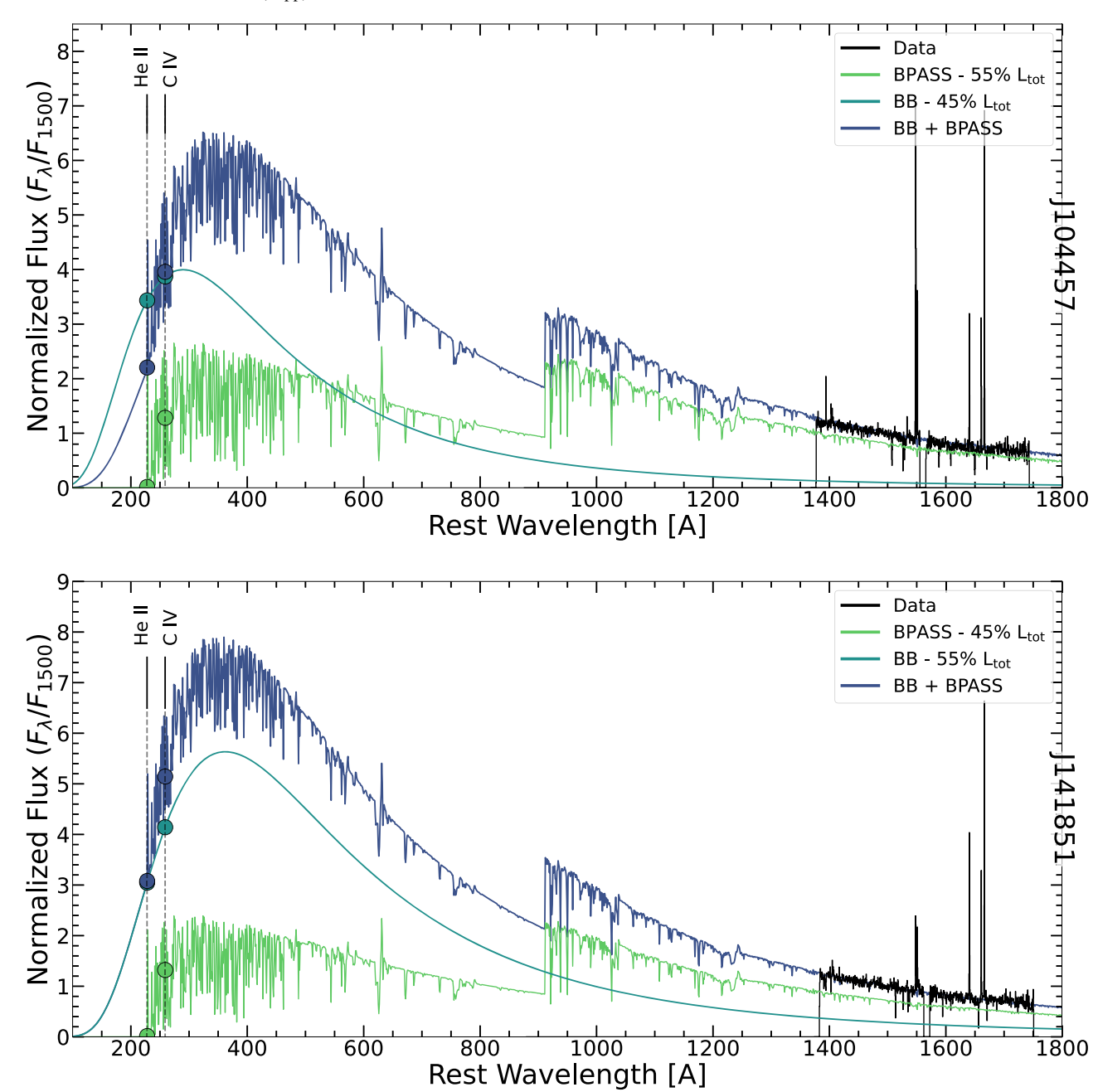


**Figure 8.** The ionizing continuum from the stellar continuum fits for the BPASS models for J104457 is shown in the top panel and for J141851 in the bottom panel. It includes a blackbody with a luminosity 45% of  $L_{tot}$  for J104457 and 55% of  $L_{tot}$  for J141851, a temperature of 80 kK, and the stellar continuum fit plus the plotted blackbody. The circles show the intersection of each model with the wavelength required to produce He II and C IV.

that binary stellar models recreate the observed UV continuum with similar precision but at slightly older ages. Even with the binary population models, we cannot reproduce the BB emission; however, binary models at lower metallicity provide more uncertainty in their models as a result of the unknown binary fractions as a function of metallicity, initial periods, and mass ratios, which are measured from the local universe but not in low-metallicity environments (Stanway et al. 2020).

Low-metallicity stellar atmospheres. These galaxies are very metal-poor. As reported in Berg et al. (2016) for J104457 and Berg et al. (2019a) for J141851, the gas in these galaxies is only 5.8% and 7.1%  $Z_{\odot}$ , respectively, and the stars themselves are only 9%–14% and 6%  $Z_{\odot}$  as reported in Table 2. The stellar population synthesis models for low-metallicity stars are

theoretical or extrapolated to lower metallicities since there are not observations of individual stars with  $Z < 0.1~Z_{\odot}$  (Lejeune et al. 1997; Gräfener et al. 2002; Smith et al. 2002; Lanz & Hubeny 2003; Topping & Shull 2015). However, stellar atmospheres are complicated structures that nonlinearly depend on the temperatures, densities, mass-loss rates, and chemical abundances. Slight variations in these parameters could produce dramatically different amounts of ionizing photons. Theoretical work on Population III stars indicates that they could provide more high-energy photons if they experienced significant mass loss (Schaerer 2002). Observations of massive stars with  $Z < 0.1~Z_{\odot}$  will provide insight as to whether low-metallicity stars are capable of producing the emission we model as a BB in this work. Telford et al. (2021,

accepted) shows that very-low-metallicity stars are not capable of producing enough high-energy photons to reproduce extreme emission lines like He II.

Very massive stars. Another option to produce our BB radiation is very massive stars, stars that are  $>100M_{\odot}$ , which could be more plausible in the low-metallicity regime. Very massive stars have been detected in SBS0335-052E by Wofford et al. (2021), who claimed the models of very massive stars reproduce the UV and optical emission lines they observed. Additionally, Senchyna et al. (2020) used a sample of 10 star-forming galaxies from SDSS to conclude that the discrepancy between stellar population models and the observed UV lines could only be rectified with additional very massive stars. When we tested both S99 and BPASS models with stellar populations up to  $300M_{\odot}$ , our ionizing continua did not sufficiently change. The ionizing continuum was larger for the  $300M_{\odot}$  models, but was not sufficient in reproducing the ionizing photons required in our BB.

Stripped stars. Another hot candidate for the source of the high-energy photons is stripped stars in binaries as suggested by Götberg et al. (2019, 2020). These stripped cores of stars are extremely hot and produce significant He II ionizing photons, but they require an older stellar population. As shown in Table 2, the stellar populations found using the UV spectra are only 1–10 Myr old. This does not preclude an older stellar population existing in these galaxies, but the young stellar population is clearly dominant in the emission lines we observe. Wide-field Infrared Survey Explorer (WISE) photometry of J104457 indicates the infrared SED is dominated by dust heated by the starburst and does not clearly show an older stellar population (Brammer et al. 2012).

Wolf-Rayet Stars. Another metallicity-dependent candidate is Wolf-Rayet (WR) stars. WR stars drive their envelopes off of the stellar core using line-driven winds, but at low metallicities, there are few metals to absorb the momentum required to accelerate the wind. In addition, we do not observe any WR bumps in our spectrum for J141851, but there is a possible C IV bump that could signify WRs present in J104457, as evidenced in the inset panels of Figure 2 as the emission lines from most of those species appear narrow and nebular in origin. The existence of some WRs in J104457 could help partially solve our missing high-energy-photon problem, but with only one WR emission line signature, it is unlikely we have a significant enough population to fully solve our problem. Finally, even when WR stars are observed in metalpoor galaxies, like IZw18 and SBS0335-052E, they do not produce enough ionizing photons at energies high enough to produce He II emission, as shown in Kehrig et al. (2015, 2018). With all of these things considered, WRs are not likely the source of our missing high-energy photons.

*AGNs.* Since these high-energy emission lines mimic those produced by AGNs, a reasonable candidate for our BB is a low-luminosity AGN. However, we ran a photoionization model with an AGN spectrum and found that this spectrum still overproduces the very-high-ionization lines when scaled so that the low-, intermediate-, and high-ionization lines match the observations, implying the spectrum is too hard to reproduce our suite of emission lines. The hardness of the AGN spectrum also implies the existence of hot gas that could be detected in the X-rays, but these dwarf galaxies are rarely observed with X-ray detections (Senchyna et al. 2017). The stellar masses of these galaxies are only  $10^{6.5-7} M_{\odot}$ , which, according to relations of the host mass to

central black hole mass like the one produced in Reines & Volonteri (2015), would imply an intermediate-mass black hole to power the AGN. Intermediate-mass black holes are notoriously difficult to observe; however, X-ray surveys including the Chandra COSMOS-Legacy survey have allowed studies to find AGNs in dwarf galaxies out to  $z \le 2.4$  (Mezcua et al. 2018). Similar radio surveys have observed compact radio sources consistent with AGN activity in dwarf galaxies (Reines et al. 2020), and through resolved emission line studies from the optical (Moran et al. 2014; Mezcua & Domínguez Sánchez 2020). Mezcua et al. (2018) suggested that the AGN fraction decreases to  $\sim 0.4\%$  for dwarf galaxies with stellar masses in the range of  $10^9 < M_* \le 3 \times 10^9 \ M_\odot$  with respect to both X-ray luminosity and stellar mass, which makes our  $\sim 10^{6.7} \ M_\odot$  galaxies unlikely to have AGNs driving their emission lines.

Ultraluminous X-ray Sources. Black holes could still cause the He II emission we see if they are in the form of high-mass X-ray binaries or ultraluminous X-ray sources (ULXs) where a black hole or neutron star is in a binary with an O- or B-type star and accretes material from the stellar wind of the companion. These accreting compact objects could produce the photons necessary to excite He II as suggested in Schaerer et al. (2019); however, the spectral shape of high-mass X-ray binaries is debated. Senchyna et al. (2020) found the ULX spectrum to be too hard for most small metal-poor galaxies, as these galaxies do not tend to show X-ray detections in the highenergy bands that are usually produced by ULXs. Recently, however, Simmonds et al. (2021) performed a similar analysis using ULX spectra based on observed ULXs in nearby galaxies and found that the softer spectra are capable of reproducing He II emission, but they included the caveat that ULX spectra as a whole are not well understood. In particular, Schaerer et al. (2019) proposed the He II emission from IZw18 was produced by X-ray binaries; however, when Kehrig et al. (2021) explored the feasibility of this claim, they found a separation of  $\sim 200$  pc between the high-mass X-ray binary and the He II emission, again suggesting the X-ray binary is not responsible for the He II emission observed.

Supersoft X-ray Sources. As ULXs are too hard, perhaps the younger sibling of compact object accretion, supersoft X-ray sources (SSSs), where a white dwarf (WD) accretes material, could be the physical mechanism behind the high-energy photons we require. SSSs have temperatures of  $\sim$ 10–100 eV and bolometric luminosities of  $\sim 10^{36}$ – $10^{38}$  erg s<sup>-1</sup> and so, could possibly provide the very-high-energy photons we need (Greiner et al. 1991; Kahabka et al. 1994). SSSs have not been observed in similar galaxies to date; however, the spectrum of these accreting WDs should fall into a similar parameter space as our BB. SSSs are rarely observed in nebulae similar to those found in J104457 and J141851 (Woods & Gilfanov 2016), and, as they are often viewed as the progenitors for Type Ia supernovae (SNe), it is important to note that Type Ia SNe are rarely found in low-metallicity environments (Kobayashi et al. 1998). Additionally, the presence of WDs implies an older stellar population than we observe in the UV, and as mentioned with the stripped stars, the IR information from WISE does not provide enough information to conclude whether there is an older stellar population residing in these galaxies. Even with an older stellar population, we would need  $\sim$ 50,000 and  $\sim$ 10,000 SSSs for J104457 and J141851, respectively, to produce the luminosity of our BB (J104457:  $5.1 \times 10^{42} \text{erg s}^{-1}$ ; J141851:  $1.1 \times 10^{42} \text{erg s}^{-1}$ ). The spatial distribution of these SSSs would be random in the location where the

older stellar population formed, so a spatial analysis of the He II emission could help determine if SSSs provide the very-high-energy photons we require.

Shocks. Shocks are another suggestion to produce the highenergy photons we need. Similar galaxies, IZw18 and SBS0335-052E, have soft X-ray emission that could correspond to shocks, but when the soft X-ray emission is integrated, it does not account for enough energy to produce the He II observed in those galaxies (Kehrig et al. 2015, 2018, 2021). However, models of radiative shocks with velocities  $\sim 400-500 \text{ km s}^{-1}$  are capable of producing small amounts of X-ray radiation while producing mostly extreme UV radiation, as shown in Allen et al. (2008). These models show that shocks should also produce emission lines from species like [Ne V] up to a line ratio of [Ne V]  $\lambda 3426/H\beta < 0.3$ for a shock propagating through a medium with density  $N_e = 1$ cm<sup>-3</sup> (Izotov et al. 2012). We have detections for the [Ne V]  $\lambda 3426$  line from both J104457 and J141851, and the [Ne V]  $\lambda 3426/H\beta$  ratio for J104457 [Ne V]  $\lambda 3426/H\beta$  is only 0.0011 and for J141851 [Ne V]  $\lambda 3426/H\beta = 0.0060$ . These ratios are much smaller than the predicted models for shocks from Izotov et al. (2012). Izotov et al. (2012) also found that the shock models overpredicted the emission line intensities if the shocks had speeds of  $>200 \text{ km s}^{-1}$ . To solve this, they required that the shocks only contribute <10% of the stellar ionizing radiation. Additionally, Berg et al. (2018) tested models with shock emission combined with BPASS binary stellar population models to explain the extreme He II emission from the lensed star-forming galaxy SL2S J021737-051329 at  $z \sim 2$  and found that shocks generally produced too little C III] emission and overpredicted most other line ratios when the He II/C III] ratio was reproduced.

Catastrophic Cooling. Finally, suppressed super winds causing catastrophic cooling could cause very-high-energy ionization line emission, as suggested by Gray et al. (2019) and Danehkar et al. (2021). In this case, the rapid gas cooling through lines like O VI creates extreme emission beyond the capabilities of the stellar population. Gray et al. (2019) predicted significant He II emission at the outer boundary of their nebula, and Danehkar et al. (2021) predicted O VI emission from the central parts of the nebula. Future work with spatially resolved He II emission could help determine if these confined winds are the source of the additional high-energy photons we observe. Additionally, future observations of these galaxies should look for emission lines indicative of this catastrophic cooling such as Si III  $\lambda$ 1206 and O VI  $\lambda$ 1037. We examined existing low-resolution spectra for O VI for J104457 and J141851 and found that O VI is not significantly detected.

This is an incomplete list of possible candidates that could generate the high-energy photons we infer. Future work can help determine which mechanism provides the very-high-energy photons. Spatial resolution of the He II emission and observations of the X-rays produced by J104457 and J141851 will help rule out some of the options provided in this list. We hope that by providing a BB with temperature and percentage of the young stellar population  $L_{\rm young}$ , we are laying down a foundation for building a physical model of the source of the high-energy photons.

# 6. Conclusions

We used the HST/COS and LBT/MODS spectra presented in Paper I to study the stellar populations and extreme emission lines from two EELGs, J104457 and J141851. These EELGs

have the largest reported C IV and He II EWs in the local universe, which suggests these are likely reionization analog galaxies. We fit the stellar populations for these galaxies using the UV continuum from the HST/COS spectrum and find these are very young stars with ages  $\leqslant 10$  Myr and that are metalpoor with metallicities  $\leqslant 0.15~Z_{\odot}$ . We used photoionization modeling to check if (a) single-age bursts of star formation, (b) the stellar populations from the UV continuum fits, and (c) an additional BB component combined with the observationally motivated stellar populations were capable of reproducing the emission lines observed in these EELGs.

Our specific results from this work are as follows:

- 1. The stellar populations that dominate the continuum in UV spectra are extremely young and metal-poor. We used the methods set up in Chisholm et al. (2019) to measure the age and metallicity of the stellar populations in J104457 and J141851 and found ages of  $4.01\pm1.13\,\mathrm{Myr}$  and  $3.37\pm1.24\,\mathrm{Myr}$ , respectively. The metallicities were measured at  $0.09\pm0.05\,Z_\odot$  and  $0.06\pm0.05\,Z_\odot$  for J104457 and J141851, respectively. We used both single-star and binary-star models and models with high-mass cutoffs at  $300M_\odot$  in addition to models with high-mass cutoffs at  $100M_\odot$ . The use of very massive star models did increase the ionizing photon production rate but did not account for the increase needed to produce the extreme He II we observe.
- 2. Absorption features in the UV continuum also indicate young stellar populations. We found Fe V and S V absorption features in the UV continuum for both J104457 and J141851. These features are indicative of young stellar populations in higher-metallicity galaxies, but their observation in these low-metallicity stellar populations confirms the presence of very hot stellar atmospheres, which require young massive stars.
- 3. We used photoionization modeling with CLOUDY to test whether single-age bursts of star formation could reproduce the observed emission lines from our EELGs. We find that BPASS single-age burst models match the emission lines from species in the low- and intermediate-ionization zones, but do not produce enough high-ionization photons to recreate the high- and very-high-ionization lines, including O III], [Ar IV], [Ne III], He II, and O IV]. These models are frequently used to model the stellar populations found in EELGs, but they are insufficient to reproduce the high-ionization emission lines from EELGs.
- 4. We used the stellar populations fit in Section 3 as inputs for our photoionization modeling with CLOUDY in an attempt to reproduce all emission lines with the stars observed in the galaxy. Although our observationally motivated stellar models were able to reproduce the low-, intermediate-, and high-ionization lines, the very-high-ionization lines like [Ne III], He II, and O IV] were still out of reach for these models. The inability of the observed stars to reproduce the observed emission indicates there is an additional source of very-high-energy ionizing photons produced in these galaxies.
- 5. We added our observationally motivated stellar population from Section 3 to a BB of temperature 80 kK that contributes 45% and 55% of the bolometric luminosity from the young stars for J104457 and J141851, respectively. This ad hoc BB produces the very-high-energy photons required to reproduce the very-high-ionization lines like [Ne III],

He II, and O IV]. The combination of BB and observed stellar population models is capable of reproducing the entire suite of emission lines, from low-ionization [O II] up to very-high-ionization O IV].

- 6. The HEIP<sup>3</sup> is often seen in EELGs where the extreme emission lines like He II and O IV] cannot be reproduced by the stellar populations expected to reside there or by other combinations of physical phenomena like collections of WR stars or ULXs. The ad hoc BB we used to model the high-energy photons needed to produce the observed He II solves the HEIP<sup>3</sup> for the two EELGs studied in this paper by simultaneously reproducing the suite of emission lines across all ionization zones from low to very high.
- 7. The BB we add to our observationally motivated stellar models could come from a number of physical sources, but we are unsure which sources would produce this set of ionizing photons. Some of the previously suggested solutions from the literature include shocks, WR stars, very massive stars, and ULXs. We address these previous physical suggestions in Section 5.3, but none of the possible solutions stands out as a clear explanation of our high-energy photons. We require further observations at additional wavelengths to test more of these suggestions.

We have listed numerous possibilities of physical sources that could produce the high-energy photons needed to explain the very-high-ionization lines in J104457 and J141851. Further exploration of these galaxies in the X-ray could help limit the options by exploring the range of photons at high energies. Additional information from spatially resolved He II emission would provide information that could help determine if the source of the ionizing photons is centrally located or if it exhibits a larger spatial distribution. Further UV spectroscopy could be useful in searching for O VI signatures related to some of the possible suggestions. We leave these explorations of J104457 and J141851 to future work.

G.M.O. is thankful for the support for this program HST-GO-15465, which was provided by NASA through a grant from the Space Telescope Science Institute, which is operated by the Association of Universities for Research in Astronomy, Inc., under NASA contract NAS5-26555. D.K.E. is supported by the US National Science Foundation (NSF) through Astronomy & Astrophysics grant AST-1909198.

This paper made use of the modsIDL spectral data reduction reduction pipeline developed in part with funds provided by NSF grant AST-1108693 and a generous gift from OSU Astronomy alumnus David G. Price through the Price Fellowship in Astronomical Instrumentation.

This work uses observations obtained with the Large Binocular Telescope (LBT). The LBT is an international collaboration among institutions in the United States, Italy, and Germany. LBT Corporation partners are: The University of Arizona on behalf of the Arizona Board of Regents; Istituto Nazionale di Astrofisica, Italy; LBT Beteiligungsgesellschaft, Germany, representing the Max-Planck Society, The Leibniz Institute for Astrophysics Potsdam, and Heidelberg University; The Ohio State University, representing OSU, University of Notre Dame, University of Minnesota and University of Virginia.

Facilities: LBT (MODS), HST (COS).

*Software:* CLOUDY (C17.01; Ferland et al. 2017), MODSIDL (Croxall & Pogge 2019).

# Appendix A Additional Emission Line Plots

In Sections 4.2.2 and 4.2.3 we used 10 emission lines to find the best-fit photoionization model from CLOUDY; however, we only presented five representative emission lines in Figure 5. We present the plots for the remaining five emission lines we used in the CLOUDY fits from Section 4.2.2 and Section 4.2.3 in Figure A1.

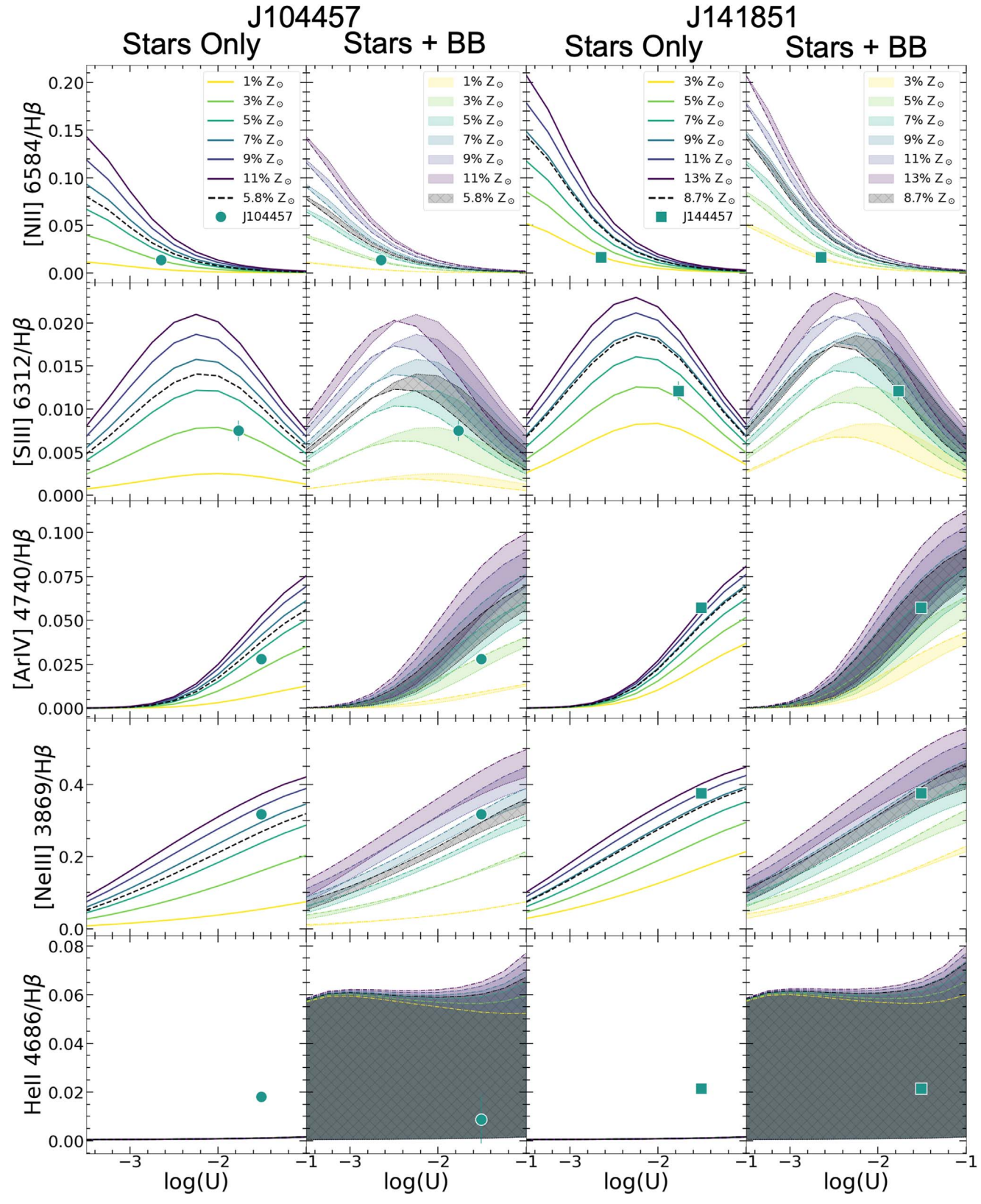


Figure A1. The same as Figure 5 but showing the line ratio diagrams for the other five emission lines spanning the different ionization zones with the observed line ratio plotted as the point for J104457 and J141851. The "Stars Only" column shows the CLOUDY photoionization models where we used the ionizing continuum from the stellar population we fit to these galaxies in Section 3.2 as the input ionizing spectrum. Each line is a different metallicity from low metallicity at  $1\% Z_{\odot}$  in yellow to  $11\% Z_{\odot}$  in purple for J104457, and for J141851 the range starts with  $3\% Z_{\odot}$  in yellow and goes to  $13\% Z_{\odot}$  in purple. The black dashed line shows the results of a model run with the observed gas-phase metallicity of each galaxy,  $5.8\% Z_{\odot}$  for J104457 and  $8.7\% Z_{\odot}$  for J141851. In the "Stars + BB" column, the models are plotted in bands with the same metallicity color-coding system, but the bands now include the effects of the blackbodies we modeled. The band is bordered by a dotted line showing the  $0\% L_{\rm tot}$  (no BB) model and a dashed–dotted line showing the  $75\% L_{\rm tot}$  from a 100 kK blackbody. The black hatched region shows the models run with the observed gas-phase metallicity of the galaxy.

# Appendix B Additional Very-high-energy Lines

There are additional emission lines that could help constrain the blackbody contribution in galaxies J104457 and J141851. These lines include both [Ne V] and [Fe V], which are both present in the spectra presented in Figure 2 and that we measured in Paper I. We did not use these two lines in the main body of our work for two main reasons: (1) [Ne V] is in the very blue part of the LBT/MODS spectrum, and the continuum measurements in this part of the spectrum are not well known; as such, the errors on [Ne V] are large, and we do not trust the measurement of this emission line as much. (2) [Fe V] requires a well-known iron abundance, of which Paper I demonstrated four different ionization correction factors result in different iron abundances all of which were measured from the same galaxies.

Nevertheless, we add these two emission lines to our suite of emission lines used to fit the CLOUDY models to our observations in this Appendix. We only add [Ne V] 3426 to the models from Section 4.2.1 as the iron abundances were not modified in the large grid of models, and thus the [Fe V] emission would likely not match. For the models from Section 4.2.2 and Section 4.2.3 we added both the [Ne V] and the [Fe V] emission lines to our suite of lines. The results of these fits are presented in Tables B1 and B2. The models are

compared to the emission lines for [Ne V] and [Fe V] in Figures B1 and B2.

We find that the addition of [Ne V] and [Fe V] to the emission line suite for fitting only changes the results of the best-fit blackbody more for J104457. The additional high-energy emission lines are small, and the models for the [Fe V] emission are much larger than the observation for most models. As such, the fitting process chooses a slightly lower log U and a lower BB percentage for J104457 for the very-high-emission line suite. The addition of [Ne V] and [Fe V] only changes the J104457 BB component to an 80,000 K BB with 35%  $L_{\rm young}$  instead of 80,000 K with 45%  $L_{\rm young}$  with only 10 emission lines. The models are not as high for J141851, and thus the very-high-energy fits choose a similar BB percentage with a lower log U. The full suite of 12 emission lines chooses the same BB component as the 10 emission line suite of an 80,000 K BB producing 55% of  $L_{\rm young}$  for J141851.

Focusing only a few emission lines can change the part of the SED we observe and change our interpretation of the sources in our galaxies. By adding these very-high-energy lines to our entire suite, we can see that the additional source does not significantly change by including these very-high-energy lines. The suite of emission lines lets us trace the shape of the ionizing continuum in our galaxies rather than probing only a small portion of the SED using only a single emission line.

**Table B1**J104457 Fit Parameters

Model	Ionization Zone				J104457 =	= 0.058 Z <sub>☉</sub>			
Section	and (Lines Used)	$\chi^2$	$\log U$	$Z(Z_{\odot})$	Age (Myr)	$\frac{C/O}{(C/O)_{\odot}}$	$\frac{N/O}{(N/O)_{\odot}}$	Temp (kK)	BB %
4.2.1	Low ([O II], [N II])	0.29	-2.5	0.05	5.01	0.25	0.25	•••	
Single-aged Burst	Inter. ([S III], [Ar III])	0.71	-3.0	0.05	10.0	1.25	1.25		
Binary Models	High ([O III], [Ar IV], [Ne III]) V. High (He II,He II,	34.52	-1.0	0.05	1.0	0.25	0.25		•••
	O IV], [Ne V])	293.91	-1.0	0.15	3.16	0.25	0.25		
	All 11	137.51	-1.0	0.15	3.16	1.25	1.25	•••	•••
4.2.2	Low ([O II], [N II])	2.02	-2.5	0.05	4.01	0.34	0.32		
Stellar Population	Inter. ([S III], [Ar III])	1.09	-3.25	0.05	4.01	0.34	0.32		
Fit Models	High ([O III], [Ar IV], [Ne III]) V. High (He II,He II,	31.37	-1.75	0.07	4.01	0.34	0.32		•••
	O IV], [Ne V], [Fe V])	291.25	-1.0	0.01	4.01	0.34	0.32	•••	
	All 12	145.34	-1.75	0.07	4.01	0.34	0.32	•••	•••
4.2.3	Low ([O II], [N II])	1.81	-2.25	0.058	4.01	0.34	0.32	60	75
Combination Stellar +	Inter.([S III], [Ar III])	2.92	-3.5	0.058	4.01	0.34	0.32	60	0
Blackbody Models	High ([O III], [Ar IV],[Ne III]) V. High (He II,He II,	57.76	-1.5	0.058	4.01	0.34	0.32	60	75
	O IV], [Ne V], [Fe V])	13.81	-2.25	0.058	4.01	0.34	0.32	80	35
	All 12	33.25	-1.75	0.058	4.01	0.34	0.32	80	35

Note. J104457 parameters of best-fit stellar population and gas from models described in Appendix B to show the addition of [Ne V] for all models and [Fe V] to the Section 4.2.2 and 4.2.3 models. All parameter values in *italics* denote that the parameter value was fixed for the model. In the Section 4.2.2 models the fixed parameters are the age, (C/O), and (N/O) ratios, 4.2.2 and for the Section 4.2.3 models the metallicity, age, (C/O), and (N/O) ratios were fixed. 4.2.3 Photoionization models from Section 4.2.1 use single-age bursts of star formation from BPASS v2.1 as the input spectrum with gas metallicities fixed to the same as the stars, but variable (C/O) and (N/O) ratios. Models from Section 4.2.2 use the ionizing continuum from Section 3.2 as the input spectrum with gas-phase metallicities varying around the gas-phase metallicity measured in Paper I, and (C/O) and (N/O) ratios fixed to the abundances from Paper I. The models from Section 4.2.3 use the ionizing continuum from Section 3.2 plus an ad hoc blackbody as the input spectrum with fixed gas-phase metallicity and (C/O) and (N/O) ratios as measured with the four-zone abundances in Paper I.

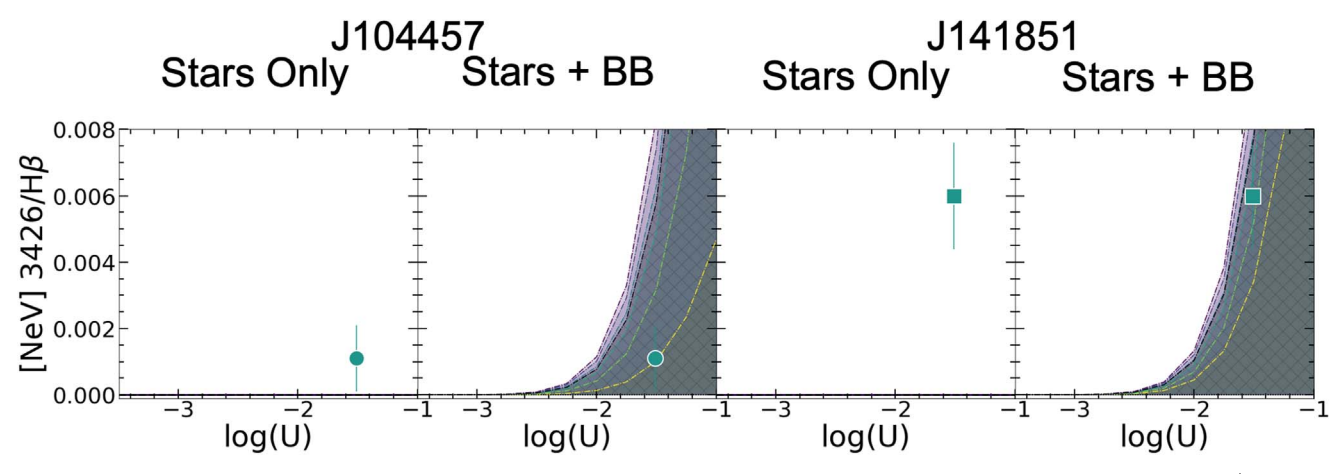
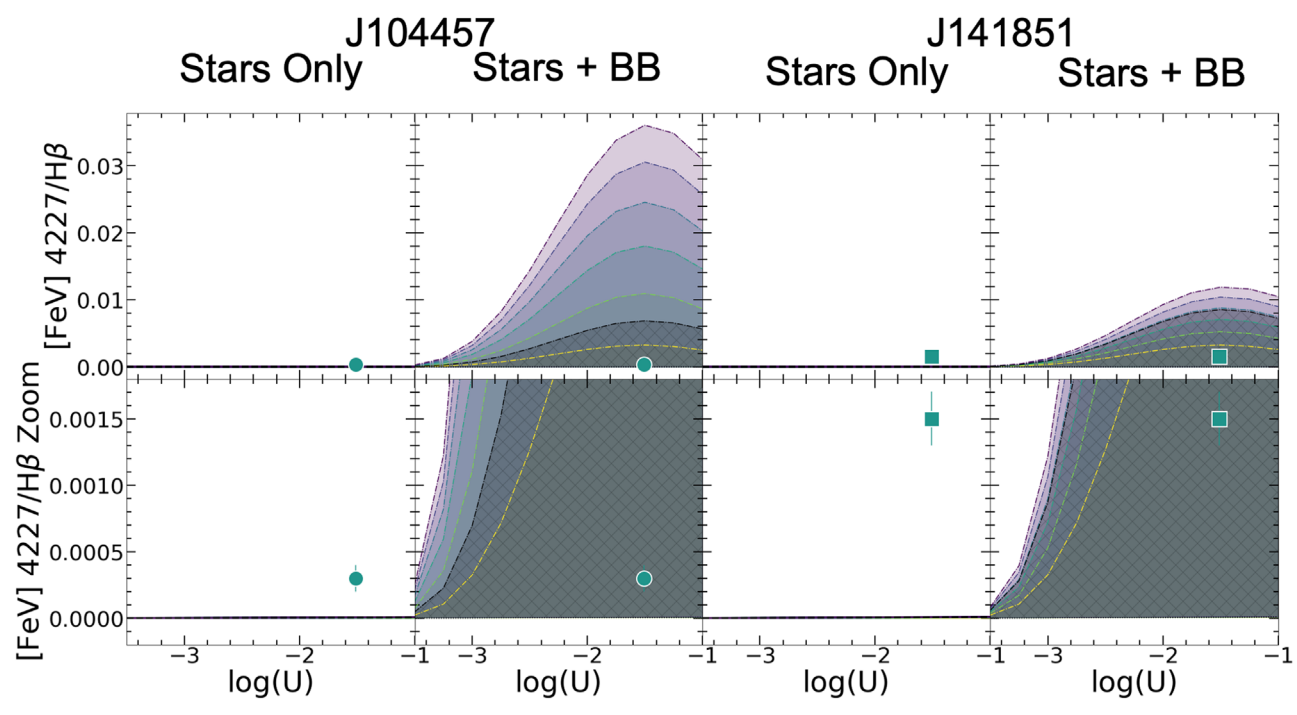


Figure B1. Similar to Figure 5 but showing the [Ne V]  $\lambda 3426$  emission line and the models we tested in Appendix B, which include the [Ne V]/H $\beta$  line ratio to constrain the very-high-energy photons with energies  $> \sim 100$  eV. The models with the added BB component sharply increase at high log U values and are able to reach the observed emission line ratio for both galaxies.

**Table B2**J141851 Fit Parameters

Model	Ionization Zone				J141851 =	$= 0.087~Z_{\odot}$			
Section	and (Lines Used)	$\chi^2$	$\log U$	$Z(Z_{\odot})$	Age (Myr)	$\frac{C/O}{(C/O)_{\odot}}$	$\frac{N/O}{(N/O)_{\odot}}$	Temp (kK)	BB %
4.2.1	Low ([O II], [N II])	17.54	-2.25	0.1	3.16	0.25	0.25		
Single-aged Burst	Inter. ([S III], [Ar III])	0.01	-1.25	0.15	5.01	0.5	0.5		
Binary Models	High ([O III], [Ar IV], [Ne III]) V. High (He II,He II,	230.90	-1.0	0.1	1.0	0.75	0.75		•••
	O IV],[Ne V])	468.15	-1.0	0.15	3.16	0.25	0.25		
	All 11	288.53	-1.0	0.15	3.16	1.25	1.25	•••	
4.2.2	Low ([O II], [N II])	51.25	-2.25	0.07	3.37	0.31	0.40		
Stellar Population	Inter. ([S III], [Ar III])	1.02	-2.5	0.05	3.37	0.31	0.40		
Fit Models	High ([O III],[Ar IV], [Ne III]) V. High (He II,He II,	19.85	-1.25	0.07	3.37	0.31	0.40		•••
	O IV],[Ne V], [Fe V])	459.67	-1.0	0.03	3.37	0.31	0.40		
	All 12	262.65	-1.75	0.11	3.37	0.31	0.40		•••
4.2.3	Low ([O II], [N II])	68.93	-2.25	0.087	3.37	0.31	0.40	80	70
Combination Stellar +	Inter.([S III], [Ar III])	4.30	-1.75	0.087	3.37	0.31	0.40	100	5
Blackbody Models	High ([O III], [Ar IV], [Ne III]) V. High (He II,He II,	19.84	-1.75	0.087	3.37	0.31	0.40	100	50
	O IV], [Ne V], [Fe V])	3.35	-2.0	0.087	3.37	0.31	0.40	80	55
	All 12	53.47	-1.75	0.087	3.37	0.31	0.40	80	55

Note. Same as Table B1 but for J141851. All parameter values in *italics* denote that the parameter value was fixed for the model. In the Section 4.2.2 models the fixed parameters are the age, (C/O), and (N/O) ratios, 4.2.2 and for the Section 4.2.3 models the metallicity, age, (C/O), and (N/O) ratios were fixed. 4.2.3



**Figure B2.** Similar to Figure 5 but this demonstrates the [Fe V]  $\lambda$ 4227 emission line ratios and the models we used in Appendix B. The models without an additional source do not reproduce the observed emission lines, but an added BB source does enable the models to reach the observations. These models greatly overpredict the emission line ratios we observe from [Fe V], so we show a cropped version of the plot in the bottom row to show observations more clearly.

## ORCID iDs

Grace M. Olivier https://orcid.org/0000-0002-4606-4240
Danielle A. Berg https://orcid.org/0000-0002-4153-053X
John Chisholm https://orcid.org/0000-0002-0302-2577
Dawn K. Erb https://orcid.org/0000-0001-9714-2758
Richard W. Pogge https://orcid.org/0000-0003-1435-3053
Evan D. Skillman https://orcid.org/0000-0003-0605-8732

References Allen, M. G., Groves, B. A., Dopita, M. A., Sutherland, R. S., & Kewley, L. J. 2008, ApJS, 178, 20 Asplund, M., Grevesse, N., Sauval, A. J., & Scott, P. 2009, ARA&A, 47, 481 Atek, H., Richard, J., Kneib, J.-P., & Schaerer, D. 2018, MNRAS, 479, 5184 Atek, H., Siana, B., Scarlata, C., et al. 2011, ApJ, 743, 121 Bayliss, M. B., Rigby, J. R., Sharon, K., et al. 2014, ApJ, 790, 144 Berg, D. A., Chisholm, J., Erb, D. K., et al. 2019b, ApJL, 878, L3 Berg, D. A., Chisholm, J., Erb, D. K., et al. 2021, ApJ, 922, 170 Berg, D. A., Erb, D. K., Auger, M. W., Pettini, M., & Brammer, G. B. 2018, pJ, 859, 164 Berg, D. A., Erb, D. K., Henry, R. B. C., Skillman, E. D., & McQuinn, K. B. W. 2019a, ApJ, 874, 93 Berg, D. A., Skillman, E. D., Croxall, K. V., et al. 2015, ApJ, 806, 16 Berg, D. A., Skillman, E. D., Henry, R. B. C., Erb, D. K., & Carigi, L. 2016, J. 827, 126 Berg, D. A., Skillman, E. D., Marble, A. R., et al. 2012, ApJ, 754, 98 Bouwens, R., González-López, J., Aravena, M., et al. 2020, ApJ, 902, 112 Bouwens, R. J., Illingworth, G. D., Oesch, P. A., et al. 2015, ApJ, 803, 34 Brammer, G. B., Sánchez-Janssen, R., Labbé, I., et al. 2012, ApJL, 758, L17 Bruhweiler, F. C., Kondo, Y., & McCluskey, G. E. 1981, ApJS, 46, 255 Calzetti, D., Armus, L., Bohlin, R. C., et al. 2000, ApJ, 533, 682 Cardelli, J. A., Clayton, G. C., & Mathis, J. S. 1989, ApJ, 345, 245 Chevallard, J., Charlot, S., Senchyna, P., et al. 2018, MNRAS, 479, 3264 Chisholm, J., Rigby, J. R., Bayliss, M., et al. 2019, ApJ, 882, 182 Christensen, L., Møller, P., Fynbo, J. P. U., & Zafar, T. 2014, MNRAS, 445, 225 Croxall, K. V., & Pogge, R. W. 2019, rwpogge/modsIDL: modsIDL Binocular Release, Zenodo, doi:10.5281/zenodo.2561424 Danehkar, A., Oey, M. S., & Gray, W. J. 2021, ApJ, 921, 91 Eldridge, J. J., Stanway, E. R., Xiao, L., et al. 2017, PASA, 34, e058

```
Feltre, A., Charlot, S., & Gutkin, J. 2016, MNRAS, 456, 3354
Ferland, G. J., Chatzikos, M., Guzmán, F., et al. 2017, RMxAA, 53, 385
Finkelstein, S. L., Ryan, R. E. J., Papovich, C., et al. 2015, ApJ, 810, 71
Gordon, K. D., Clayton, G. C., Misselt, K. A., Landolt, A. U., & Wolff, M. J.
   2003, ApJ, 594, 279
Götberg, Y., de Mink, S. E., Groh, J. H., Leitherer, C., & Norman, C. 2019,
     &A, 629, A134
Götberg, Y., de Mink, S. E., McQuinn, M., et al. 2020, A&A, 634, A134
Gräfener, G., Koesterke, L., & Hamann, W. R. 2002, A&A, 387, 244
Grasha, K., Roy, A., Sutherland, R. S., & Kewley, L. J. 2021, ApJ, 908, 241
Gray, W. J., Oey, M. S., Silich, S., & Scannapieco, E. 2019, ApJ, 887, 161
Green, G. M., Schlafly, E. F., Finkbeiner, D. P., et al. 2015, ApJ, 810, 25
Greiner, J., Hasinger, G., & Kahabka, P. 1991, A&A, 246, L17
Guseva, N. G., Izotov, Y. I., & Thuan, T. X. 2000, ApJ, 531, 776
Hainline, K. N., Shapley, A. E., Kornei, K. A., et al. 2009, ApJ, 701, 52
Harikane, Y., Ouchi, M., Inoue, A. K., et al. 2020, ApJ, 896, 93
Heckman, T. M., Alexandroff, R. M., Borthakur, S., Overzier, R., &
   Leitherer, C. 2015, ApJ, 809, 147
Hill, J. M., Green, R. F., Ashby, D. S., et al. 2010, Proc. SPIE, 7733, 77330C
Izotov, Y. I., Schaerer, D., Thuan, T. X., et al. 2016, MNRAS, 461, 3683
Izotov, Y. I., Thuan, T. X., & Privon, G. 2012, MNRAS, 427, 1229
Izotov, Y. I., Worseck, G., Schaerer, D., et al. 2018, MNRAS, 478, 4851
James, B. L., Pettini, M., Christensen, L., et al. 2014, MNRAS, 440, 1794
Jaskot, A. E., Oey, M. S., Scarlata, C., & Dowd, T. 2017, ApJL, 851, L9
Kahabka, P., Pietsch, W., & Hasinger, G. 1994, A&A, 288, 538
Kehrig, C., Guerrero, M. A., Vílchez, J. M., & Ramos-Larios, G. 2021, ApJL,
   908, L54
Kehrig, C., Vílchez, J. M., Guerrero, M. A., et al. 2018, MNRAS, 480, 1081
Kehrig, C., Vílchez, J. M., Pérez-Montero, E., et al. 2015, ApJL, 801, L28
Kobayashi, C., Tsujimoto, T., Nomoto, K., Hachisu, I., & Kato, M. 1998,
   ApJL, 503, L155
Kroupa, P. 2002, Sci, 295, 82
Lanz, T., & Hubeny, I. 2003, ApJS, 146, 417
Leitherer, C., Tremonti, C. A., Heckman, T. M., & Calzetti, D. 2011, AJ,
Leitherer, C., Schaerer, D., Goldader, J. D., et al. 1999, ApJS, 123, 3
Lejeune, T., Cuisinier, F., & Buser, R. 1997, A&AS, 125, 229
Livermore, R. C., Finkelstein, S. L., & Lotz, J. M. 2017, ApJ, 835, 113
Madau, P., & Haardt, F. 2015, ApJL, 813, L8
Mainali, R., Kollmeier, J. A., Stark, D. P., et al. 2017, ApJL, 836, L14
Mainali, R., Zitrin, A., Stark, D. P., et al. 2018, MNRAS, 479, 1180
Maseda, M. V., van der Wel, A., da Cunha, E., et al. 2013, ApJL, 778, L22
Maseda, M. V., van der Wel, A., Rix, H.-W., et al. 2014, ApJ, 791, 17
```

```
Meynet, G., Maeder, A., Schaller, G., Schaerer, D., & Charbonnel, C. 1994,
   A&AS, 103, 97
Mezcua, M., Civano, F., Marchesi, S., et al. 2018, MNRAS, 478, 2576
Mezcua, M., & Domínguez Sánchez, H. 2020, ApJL, 898, L30
Moran, E. C., Shahinyan, K., Sugarman, H. R., Vélez, D. O., & Eracleous, M.
   2014, AJ, 148, 136
Oesch, P. A., Bouwens, R. J., Illingworth, G. D., Labbé, I., & Stefanon, M.
   2018, ApJ, 855, 105
Oke, J. B. 1990, AJ, 99, 1621
Pogge, R. W., Atwood, B., Brewer, D. F., et al. 2010, Proc. SPIE, 7735,
   77350A
Reddy, N. A., Steidel, C. C., Pettini, M., Bogosavljević, M., & Shapley, A. E.
   2016, ApJ, 828, 108
Reines, A. E., Condon, J. J., Darling, J., & Greene, J. E. 2020, ApJ, 888, 36
Reines, A. E., & Volonteri, M. 2015, ApJ, 813, 82
Rigby, J. R., Bayliss, M. B., Chisholm, J., et al. 2018b, ApJ, 853, 87
Rigby, J. R., Bayliss, M. B., Gladders, M. D., et al. 2015, ApJL, 814, L6
Rigby, J. R., Bayliss, M. B., Sharon, K., et al. 2018a, AJ, 155, 104
Robertson, B. E., Ellis, R. S., Furlanetto, S. R., & Dunlop, J. S. 2015, ApJL,
   802, L19
Schaerer, D. 2002, A&A, 382, 28
Schaerer, D., Fragos, T., & Izotov, Y. I. 2019, A&A, 622, L10
```

Senchyna, P., Stark, D. P., Mirocha, J., et al. 2020, MNRAS, 494, 941

```
Senchyna, P., Stark, D. P., Vidal-García, A., et al. 2017, MNRAS, 472, 2608
Simmonds, C., Schaerer, D., & Verhamme, A. 2021, A&A, 656, A127
Smith, L. J., Norris, R. P. F., & Crowther, P. A. 2002, MNRAS, 337, 1309
Stanway, E. R., Chrimes, A. A., Eldridge, J. J., & Stevance, H. F. 2020,
  MNRAS, 495, 4605
Stanway, E. R., & Eldridge, J. J. 2018, MNRAS, 479, 75
Stanway, E. R., & Eldridge, J. J. 2019, A&A, 621, A105
Stanway, E. R., Eldridge, J. J., & Becker, G. D. 2016, MNRAS, 456, 485
Stark, D. P. 2016, ARA&A, 54, 761
Stark, D. P., Richard, J., Charlot, S., et al. 2015, MNRAS, 450, 1846
Stasińska, G., Izotov, Y., Morisset, C., & Guseva, N. 2015, A&A, 576, A83
Steidel, C. C., Rudie, G. C., Strom, A. L., et al. 2014, ApJ, 795, 165
Tang, M., Stark, D. P., Chevallard, J., & Charlot, S. 2019, MNRAS, 489, 2572
Tang, M., Stark, D. P., Chevallard, J., et al. 2021, MNRAS, 501, 3238
Thuan, T. X., & Izotov, Y. I. 2005, ApJS, 161, 240
Topping, M. W., & Shull, J. M. 2015, ApJ, 800, 97
van der Wel, A., Straughn, A. N., Rix, H. W., et al. 2011, ApJ, 742, 111
van Zee, L., & Haynes, M. 2006, ApJ, 636, 214
Vink, J. S., de Koter, A., & Lamers, H. J. G. L. M. 2001, A&A, 369, 574
Wise, J. H., Demchenko, V. G., Halicek, M. T., et al. 2014, MNRAS,
  442, 2560
Wofford, A., Vidal-García, A., Feltre, A., et al. 2021, MNRAS, 500, 2908
```

Woods, T. E., & Gilfanov, M. 2016, MNRAS, 455, 1770